



Provided by the author(s) and University of Galway in accordance with publisher policies. Please cite the published version when available.

Title	Computational study on the effect of contact geometry on fretting behaviour
Author(s)	McHugh, Peter; Zhang, Teng; Lean, Sean
Publication Date	2011-07-23
Publication Information	Zhang, T., McHugh, P. E., & Lean, S. B. (2011). Computational study on the effect of contact geometry on fretting behaviour. <i>Wear</i> , 271(9–10), 1462-1480.
Publisher	Elsevier ScienceDirect
Link to publisher's version	http://dx.doi.org/10.1016/j.wear.2010.11.017
Item record	http://hdl.handle.net/10379/5387
DOI	http://dx.doi.org/doi:10.1016/j.wear.2010.11.017

Downloaded 2024-04-17T20:19:58Z

Some rights reserved. For more information, please see the item record link above.



Computational study on the effect of contact geometry on fretting behaviour

T. Zhang^{*}, P. E. McHugh, S. B. Leen

*Department of Mechanical and Biomedical Engineering,
NUI Galway, Nun's Island, Galway, Ireland*

Received Date Line

Abstract

A key challenge in the design of engineering couplings and contacting components relates to the development of an understanding of the comparative performance of contrasting contact geometries for a given application, including loading, applied deformations and geometrical space envelope. Although fretting is observed in many mechanical assemblies such as keyway-shaft couplings, shrink-fitted couplings, one specific example which has motivated the present work is the pressure armour layer of a marine flexible riser, where the groove and nub experience fretting contact damage. A Hertzian cylinder-on-flat contact geometry is commonly assumed for this groove-nub contact due to the ready availability of the contact (normal and tangential) analytical solutions for this geometry. In reality the contact geometry is closer to a rounded punch-on-flat. The present work adopts a finite element methodology to compare the significance of the Hertzian assumption to that of a rounded punch-on-flat, in terms of fretting behaviour.

Keywords: fretting, wear, contact geometry, ratchetting, multi-axial fatigue, energy wear approach, flexible riser

1. Introduction

Fretting occurs when two contacting bodies experience small amplitude oscillatory motion. It is observed in many mechanical assemblies such as keyway-shaft couplings, shrink-fitted couplings etc. Fretting can be divided into three regimes [1] by slip amplitude, namely gross slip regime (GSR), partial slip regime (PSR) and mixed slip regime (MSR). Generally fretting can result in fretting wear and under certain conditions, especially in PSR and MSR,

^{*}Corresponding author. Tel.: +353 91 493020; fax: + 353 91 563991.
E-mail address: t.zhang2@nuigalway.ie (T. Zhang)

1 fretting fatigue occurs. Using 'fretting map' approaches, Vingsbo et al. [2] have shown that the
2 fretting damage evolution is strongly dependent on the slip amplitude.

3 A significant amount of effort has been expended on the research into fretting wear and
4 fatigue problems. Early work by Cattaneo [3] and Mindlin [4] on the combined normal and
5 tangential loading of a Hertzian geometry, specifically presenting an analytical solutions for
6 the partial slip case, has proved invaluable in the analysis and design of (Hertzian) engineering
7 contacts with respect to contact failure and fretting fatigue. More recently, a rounded punch-
8 on-flat contact problem has also been studied [5, 6] and analytical solutions have been
9 developed. Of course, the stress state associated with fretting leads to a multiaxial fatigue
10 problem. One approach adopted to predict fretting fatigue life from fretting-induced stresses
11 was the critical plane approach, e.g. Szolwinski and Farris [7]. This method searches for the
12 maximum of a fatigue damage parameter (e.g. Smith-Watson-Topper (*SWT*) fatigue parameter
13 [8]) over a number of different planes and predicts life based on the most damaging plane.

14 However, although many fretting fatigue studies focus attention on the partial slip
15 regime, where the effects of wear and material removal are commonly neglected, the present
16 work is concerned with the fretting wear performance of two contrasting, so-called simple,
17 contact geometries, across a range of slip regimes. The Archard equation [9] for sliding wear
18 has been adopted by a number of researchers. For example, McColl and co-workers [10,11]
19 developed an experimentally-validated finite element (FE) based incremental method for
20 fretting wear simulation (via material removal) and applied it to a Hertzian geometry to predict
21 the wear-induced evolution of contact geometry and the associated effect on contact surface
22 and sub-surface contact variables, such as contact pressure, slip and stresses. This work
23 highlighted the importance of wear-induced material removal prediction for capturing key
24 fretting phenomena, such as the effect of slip amplitude on evolution of multiaxial contact
25 stresses and multiaxial fatigue parameters, such as the *SWT* parameter. More recently, based
26 also on the Archard equation, Mohd Tobi et al. [12] highlighted the evolution of plastic strain
27 and the effects of incremental plasticity during the fretting wear. Friction plays a central role in
28 fretting, leading to contrasting slip regimes, for example, under the same normal load
29 conditions. In recognition of this, Fouvry et al. [13] have proposed an energy-based wear
30 approach, incorporating the effects of interfacial shear work as the significant wear parameter.
31 Experiments [13-15] have shown that this approach is superior to the Archard-based wear

1 model, in terms of ‘unifying’ wear predictions. Thus, a single energy-based wear coefficient
2 can predict across a range of fretting variables (normal load, stroke, etc), as compared with
3 load- and stroke-dependency for the Archard coefficient, e.g. see [10].

4 Madge et al. [16-18] combined the Archard wear simulation method with an FE-based,
5 multiaxial fatigue prediction to successfully predict the effect of fretting wear on fretting
6 fatigue life, with experimental validation against Hertzian and rounded punch-on-flat fretting
7 fatigue (with substrate fatigue loading) configurations for Ti-6Al-4V. A critical and
8 challenging aspect of fatigue life prediction is the separation and identification of crack
9 nucleation and crack propagation. To this end, Ding et al. [20] carried out combined
10 experimental and numerical study on a fretting wear configuration (initially Hertzian, without
11 substrate fatigue load) and successfully validated the combined wear-fatigue approach against
12 measured fretting-induced short cracks and wear scars for PSR, MSR and GSR conditions in
13 Ti-6Al-4V.

14 The present work is concerned with the problem of predicting the comparative fretting
15 performance of two contrasting contact geometries to transmit a specified normal load with a
16 specified tangential displacement cycle for a given material combination and within a specified
17 geometrical space envelope, as illustrated in Fig. 1. The objective is to understand which
18 geometry is better in terms of both wear and fatigue/cracking performance, particularly when
19 wear-induced evolution of contact geometry is accounted for.

20 One specific example which has motivated the present work is the pressure armour layer
21 of a marine flexible riser, which is designed to allow large deflections under combined torque,
22 axial and bending loads, leading to potential fretting contact damage to the groove and nub
23 contact regions, as illustrated in Fig. 2. Feret et al. [19] have presented analytical solutions for
24 the calculation of stresses and slip in structural layers of unbounded flexible pipes, without
25 explicit consideration of (i) the local contact geometry and (ii) wear effects. The present work
26 is a first step towards understanding and predicting fretting in flexible risers and other complex
27 contacts. It adopts a finite element (FE) methodology to compare the significance of the
28 Hertzian assumption to that of a rounded punch-on-flat, in terms of fretting performance. An
29 incremental wear simulation method based on the energy approach of Fouvry et al. [14] and
30 previous work [20] is adopted. A non-linear kinematic hardening plasticity formulation is
31 employed and a critical-plane, Smith-Watson-Topper approach is used to predict multiaxial

1 fretting crack nucleation. Wear evolution and crack nucleation predictions are validated against
2 existing published data for Ti-6Al-4V [20]. Under the same fretting variables (normal load,
3 stroke, etc), different contact geometries are shown to result in significant differences in
4 fretting behaviour. In order to assess this difference comparatively, this study describes the
5 prediction of evolution of contact geometry, wear, salient surface and sub-surface fretting
6 variables, including plasticity and fatigue damage parameters across a range of fretting strokes
7 for the two arrangements.

9 **2. Analytical solutions**

11 *2.1 Cylinder on flat contact*

12 The solution for stress, strain and slip fields of this contact is well known, therefore this
13 arrangement is widely used for fretting studies. As shown in Fig.1a, a normal load P and an
14 alternating tangential force $Q(t)$ (resulting in a stroke of $\pm A$) of amplitude Q_{max} are applied to
15 the cylinder specimen.

16 Consider the normal load only state. The well-known Hertzian solution [21] gives the
17 method of calculating the contact pressure distribution, the contact half width b , p_0 which is the
18 pressure at the centre of contact region, and the normal stresses due to the normal load along
19 the y-axis.

20 When the tangential load is introduced, relative slip occurs between the two contacting
21 surfaces. In gross slip situations, Q_{max} is increased to its limiting value μP , so that the cylinder
22 body is on the point of sliding. If Q_{max} is less than μP , partial slip occurs and in the central of
23 the contact region, a stick zone exists. The shear traction expressions have been presented [21].
24 For gross slip cases, the explicit formulations of stresses due to normal and tangential load are
25 given by Smith and Liu [22] and Sackfield and Hills [23].

27 *2.2 Rounded punch on flat contact*

1 A more realistic approximation of the pressure armour contacting surface in the flexible
 2 risers would be a rounded punch on flat arrangement. As shown in Fig.1*b*, a normal load P and
 3 an alternating tangential force $Q(t)$ of amplitude Q_{max} are applied to the rounded punch.

4 Ciavarella [5, 6] and Jager [24] have described the analytical solutions for this contact.
 5 Consider the normal load only state, the contact half width b and contact pressure distribution
 6 can be calculated and the expressions are shown in [6].

7 When a tangential load is introduced, if Q_{max} is smaller than the limiting value μP , partial
 8 slip is predicted to occur. Also here, a stick zone exists and c is the stick zone half width. The
 9 value of c can be calculated [6]

10 It is important to note that the above analytical solution is only applicable when $a \leq c \leq$
 11 b , which is actually quite restrictive.

12 The maximum tensile stress is calculated [6] as:

$$13 \quad \sigma_x(b,0) = 2\mu \frac{(b-a)}{AR} - 2 \frac{\mu}{\pi AR} w(c) \quad (1)$$

14 where $w(c)$ is:

$$15 \quad w(c) = -4\sqrt{b^2 - c^2} \arccos \sqrt{\frac{a+c}{2c}} + 2(b-a) \arcsin \sqrt{\frac{(b+c)(c-a)}{2c(b-a)}} + \quad (2)$$

$$16 \quad 2(a+b) \arcsin \sqrt{\frac{(b-c)(c-a)}{2c(a+b)}}$$

17 3. Computational methodology

18 3.1 FE modelling

19
 20 Three FE models are developed for the analyses of this paper, as shown in Table 1. In all

21 Table 1. Table of FE models for different fretting geometries studied.

Model	Pad type	Key dimensions	Test rig and source
RF1	Cylindrical pad	Pad radius, 6 mm	University of Nottingham test rig, e.g. [20]
RF2	Cylindrical pad	Pad radius, 50.8 mm	USAF test rig, e.g. [28]
RPF	Rounded punch pad	See Fig 1	USAF test rig, e.g. [28]

1 cases a two-dimensional, plane strain assumption has been employed. The general purpose,
2 non-linear FE code Abaqus is used for all of the analyses. The first model, RF1, is based on the
3 geometry of the University of Nottingham fretting test rig and is employed here to validate the
4 energy-based wear prediction methodology against the experimental and (modified Archard
5 method) numerical results of [20]. The second and third models, RF2 and RPF, are round-on-
6 flat and rounded punch-on-flat fretting geometries, based on the USAF test configuration of
7 Mall and co-workers from [28]. The purpose of the RF2 and RPF models is to comparatively
8 assess the predicted effect of contact geometry on the wear-fatigue-plasticity behaviour, across
9 a range of applied stroke values, as depicted in Fig. 1. All three models use the same material,
10 namely Ti-6Al-4V, but different tribological constants are employed in each, as identified from
11 the relevant test data (see Section 3.2 for description of this aspect).

12 Fig. 3 shows a schematic of the University of Nottingham fretting test rig which employs
13 a crossed cylinder on flat arrangement. Fig. 4 shows the RF1 FE model, which has a pad radius
14 of 6 mm. 2 dimensional (2D), four noded, quadrilateral, plane strain elements were used due to
15 their reliability in frictional contact analyses [10, 25]. Matched meshes were employed also to
16 prevent contact pressure fluctuations [10]. The mesh is designed to be highly refined in the
17 contact region (typical element dimension is 10 μm), to capture the complicated variation of
18 the key variables, including contact pressure, relative slip, and sub-surface stresses, and to
19 become gradually more coarse with increasing distance from the contact regions, for
20 computational efficiency. The mesh design process is particularly complicated for wear
21 simulation analyses, due to the need to allow for widening of the contact region (particularly in
22 gross slip cases) and therefore the need for consideration of moving stress concentration
23 locations, e.g. stick-slip interfaces and contact edges are typically predicted to move due to
24 wear-induced material removal.

25 Figures 5 and 6 show the RF2 and RPF FE models. The pads in these models are
26 assigned the same height and width in order to make a meaningful comparison for the same
27 nominal geometrical space envelope. The finite element mesh design follows the same
28 methodology and rationale as that of the RF1 model.

29 The contact surface interaction is defined via the finite sliding contact pair approach
30 which adopts the master-slave algorithm in Abaqus. The maximum allowable penetration
31 depth (*h-crit*) between the slave and master nodes during the the iterative solution process is set

1 to 1 μm . The minimum allowable distance between the initial coordinates of adjacent nodes on
 2 the mating contact surface (*ADJUST parameter*) is set to 0.001 μm . Coulomb friction is
 3 employed based on the Lagrange multiplier contact algorithm to ensure the exact stick
 4 condition when the shear stress less than the critical shear value according to the Coulomb
 5 friction law. These contact parameters have been identified from previous studies, e.g. see [10].

6 Detailed mesh refinement studies were carried out to achieve convergence with respect to
 7 the unworn surface tractions and sub-surface stresses for all three models, using available
 8 theoretical solutions for the unworn geometries. The comparisons between theoretical and
 9 converged FE predictions for the unworn cases are presented in the results section below.

11 3.2 Constitutive model

12
 13 The Bauschinger effect is a complex phenomenon observed in the cyclic behaviour of
 14 polycrystalline metals and single crystals and it can be explained by anisotropy of the
 15 dislocation fields from previous loading, whereby the yield stress in compressive loading is
 16 reduced relative to that in a preceding tensile (plastic) half-cycle and similarly reduced in
 17 tensile loading relative to that in a preceding compressive half-cycle. The kinematic hardening
 18 model is a simplified representation used to model this effect, which assumes that the yield
 19 stress range remains constant and equal to $2\sigma_y$, where σ_y is the yield stress, and the reduction
 20 in yield stress in the reversed direction is equal to the increment in yield stress in the preceding
 21 (opposite) loading direction. The non-linear kinematic hardening model is employed here to
 22 model the *Bauschinger* effect. The translation of the centre of the yield surface in kinematic
 23 hardening is governed by a tensor \mathbf{x} called the *backstress*, defined for non-linear hardening as
 24 follows:

$$25 \quad d\mathbf{x} = \frac{2}{3} C d\boldsymbol{\varepsilon}^P - \gamma \mathbf{x} dp \quad (3)$$

26 where the plastic strain increment, $d\boldsymbol{\varepsilon}^P$ is calculated via the flow rule, as follows:

$$27 \quad d\boldsymbol{\varepsilon}^P = d\lambda \frac{\partial f}{\partial \boldsymbol{\sigma}} = \frac{3}{2} dp \frac{\boldsymbol{\sigma}'}{\sigma_e} \quad (4)$$

$$1 \quad f = \sigma_e - \sigma_y = \left(\frac{3}{2} (\boldsymbol{\sigma}' - \mathbf{x}') : (\boldsymbol{\sigma}' - \mathbf{x}') \right)^{\frac{1}{2}} - \sigma_y \quad (5)$$

$$2 \quad dp = \left(\frac{2}{3} d\boldsymbol{\varepsilon}^P : d\boldsymbol{\varepsilon}^P \right)^{\frac{1}{2}} \quad (6)$$

3 where C is a the hardening modulus, f is the von Mises yield function, dp is the increment in
4 effective plastic strain, σ_e is the von Mises equivalent stress, $\boldsymbol{\sigma}'$ and \mathbf{x}' are the deviatoric stress
5 and backstress tensors, respectively, and σ_y is the yield stress. $d\lambda$ is the plastic multiplier,
6 which, for a von Mises equivalent stress, is equivalent to the increment in effective plastic
7 strain. The same cyclic elastic-plastic constitutive material model is employed for all three
8 geometries, corresponding to published data for Ti-6Al-4V from Benedetti et al. [27]. The
9 elastic material properties used for the cylinder and flat are: Young's modulus of 116 GPa and
10 Poisson's ratio of 0.342. It was shown in [12], using a linear kinematic hardening (LKH)
11 model, that cyclic plasticity and ratchetting effects play an important role in fretting of Ti-6Al-
12 4V, particularly when wear effects are accounted for. A non-linear kinematic hardening
13 (NLKH) formulation is used in the present fretting simulations with wear and fatigue. The
14 NLKH model is superior to the LKH model in the modelling of cyclic plasticity phenomena,
15 specifically ratchetting [26]; in particular, the LKH model is known to underestimate
16 ratchetting relative to the NLKH model. The cyclic material response is represented in Abaqus
17 using the elastic-plastic constitutive law proposed by Lemaitre and Chaboche [26]. The cyclic
18 strain-hardening behaviour is given by the following equation:

$$19 \quad \frac{\Delta\sigma}{2} - k = \frac{C}{\gamma} \tanh\left(\gamma \frac{\Delta\varepsilon_p}{2}\right) \quad (7)$$

20 where k , C , γ are the characteristic coefficients, the values of which are 840 MPa, 8976 MPa,
21 and 102, respectively, taken from Benedetti et al. [27]; k is the cyclic (initial) yield stress, and γ
22 is the rate of decay of the modulus. Fig 7 shows a comparison of the FE-predicted cyclic stress-
23 strain response and the theoretical formulation of Equation (7). The FE results are shown for
24 three discrete values of applied plastic strain range under uniaxial conditions (corresponding to
25 three different strain-controlled analyses), thus validating the FE-implementation of the Ti-
26 6Al-4V cyclic material behaviour.

1
2
3
4
5
6
7
8
9
10
11
12
13
14
15
16
17
18
19
20
21
22
23
24
25
26
27
28
29
30

3.3 Loading histories

Fig. 8 illustrates the loading history modelled to simulate the fretting cycles. 1 fretting cycle shown in Fig. 8 represents ΔN wear cycles, which will be explained in detail in section 3.4. The first step in the analysis is to apply the constant normal load P at point A, on the top of the FE model of the fretting pad (see Figs. 4 to 6). In the subsequent steps a periodic cyclic x -direction displacement of amplitude Δ is applied to the cylinder while constraining the bottom half of the flat specimen in the x and y -directions. The displacement amplitude Δ is varied for each simulation to model partial slip through to gross sliding to simulate the experimental results. To ensure uniform horizontal and vertical displacement of nodes on the top surface of the cylinder, linear constraint equations are employed. Due to the compliance effect of the experimental rig, the actual relative contact slips between the contacting components is normally less than the applied stroke 2Δ in the experiment. Therefore the displacement amplitude Δ is based on the relative slip rather than the applied stroke. For the gross sliding condition, the relative slip corresponding to the stroke applied in the experiment is determined from the width across the parallel portions of the hysteresis loop of the experiment. For the partial slip condition, the required displacement is taken as that value which gives the measured maximum tangential force.

Table 2 shows the fretting conditions to which the RF1 model is applied. These correspond to two selected test cases from the experimental programme reported in [20], Test 1 corresponding to a gross slip condition and Test 2 corresponding to a partial slip case.

Table 3 shows the range of test conditions used for the RF2 and RPF models. The normal load is held fixed at 208 N/mm, following the tests carried out in [15, 28] (and also analysed in [16], for both geometries and the stroke is varied between 7 μm and 20 μm , thus spanning from the partial slip (PS) regime into the gross slip (GS) regime for both.

1 3.4 Wear model

2

3 Previous wear simulation work by Leen and co-workers, e.g. [10, 18], was based on the
4 use of a modified Archard approach, based on the classical Archard wear equation for sliding
5 wear [9]:

$$6 \frac{V}{S} = K \frac{P}{H} \quad (8)$$

7 where V is the wear volume, S is the sliding distance, K is the wear coefficient, P is the normal
8 load and H is the hardness of the material. This approach has been implemented in the Abaqus
9 FE code, using both an external Fortran program and, more recently, an adaptive meshing
10 subroutine within Abaqus, and validated for both a high strength CrMoV aeroengine steel
11 (SuperCMV) [10] and Ti-6Al-4V alloy [20], under a range of load-stroke combinations.
12 However, it has been found that, for this approach, the wear co-efficient is dependent on load
13 and stroke, e.g. see [10]. An alternative method, referred to as the energy wear approach, has
14 been proposed by Fouvry and co-workers, e.g. [13], which considers the interfacial shear work
15 as the significant wear parameter controlling wear volume calculation. This approach has been
16 shown to be superior to the Archard-based approach in that a single wear coefficient can be
17 used across a range of fretting load-stroke combinations, specifically including both partial slip
18 and gross slip regimes. The energy wear approach can be represented by the following
19 equation:

$$20 V = \alpha \sum E \quad (9)$$

21 where α is the wear coefficient and $\sum E$ is the accumulated dissipated energy. However the
22 concept of the energy wear coefficient is that a value independent of load and stroke be
23 identified from tests across a range of loads and strokes; this is not typically possible with the
24 Archard approach. Nonetheless, it can be shown that in the gross slip regime, the two
25 approaches (in terms of predictions) are the same for an appropriate choice of Archard and
26 energy wear coefficients, i.e. $\alpha/\mu = K/H$, certainly in terms of predicted wear scar dimensions.
27 However, in the partial slip regime, when $Q < \mu P$, the two approaches will not give the same
28 results.

1 For a 2D model, at time t and position x , the local wear depth can be related to the local
 2 accumulated dissipated energy, as follows:

$$3 \quad h(x,t) = \alpha E(x,t) \quad (10)$$

4 where x is horizontal distance of a contact node from the centre of contact and $E(x,t)$ is the 2D
 5 accumulated dissipated energy, given by:

$$6 \quad E(x,t) = \int_{t=0}^t q(x,t) ds(x,t) \quad (11)$$

7 where $q(x,t)$ is the local instantaneous shear traction and $ds(x,t)$ is the local instantaneous
 8 incremental relative slip.

9 In this paper, following the FE-implementation previously developed for the Archard-
 10 based wear simulation method [16], the adaptive meshing UMESHMOTION user subroutine
 11 within Abaqus is used incrementally simulate the material removal according to the above
 12 equations, as described graphically in the flowchart of Fig. 9. Thus, for a contact node i at the
 13 m^{th} increment, equation (10) can be written as:

$$14 \quad \Delta h_{i,m} = \alpha E_{i,m} \quad (12)$$

15 where the incremental dissipated energy $E_{i,m}$ is:

$$16 \quad E_{i,m} = q_{i,m} \Delta s_{i,m} \quad (13)$$

17 where $q_{i,m}$ and $\Delta s_{i,m}$ are the shear traction and incremental slip, respectively, at node i in the m^{th}
 18 increment. Following the cycle-jumping technique used previously in the Archard-based
 19 approach to efficiently predict the accumulated wear depth and associated evolution of
 20 geometry and fretting variables, the total accumulated nodal wear h_i after a N_T fretting cycles is
 21 thus:

$$22 \quad h_i = \sum_{n=1}^{N_T / \Delta N} \sum_{m=1}^{m_{\max}} \Delta h_{i,m} \quad (14)$$

23 where m_{\max} is the maximum increment number within one fretting cycle and ΔN is the
 24 increment in fretting cycles (cycle jump) during which the fretting variables are assumed to
 25 remain constant. Caution is required to ensure that accuracy is not sacrificed. This is achieved
 26 here via ΔN sensitivity studies and comparison with measured wear data from [20]. The
 27 adaptive meshing algorithm of Abaqus applies the local wear increment for all surface nodes in
 28 two steps. First, the local wear increment is implemented by moving the surface nodes in the

1 local normal direction; this geometry update is implemented as a purely Eulerian analysis.
 2 Secondly, the material quantities (variables) are re-mapped to the new positions, by advection
 3 from the old location to the new location by solving the advection equations using a second
 4 order numerical method called the Lax-Wendroff method. These two steps cause an
 5 equilibrium loss which is corrected by solving the last time increment of the contact problem
 6 [22]. The wear analyses simulate up to 300×10^3 cycles using a cycle jump ΔN of 2×10^3 with
 7 100 increments in one simulated tangential fretting cycle.

8

9 3.5 Fatigue model

10

11 A critical plane approach incorporating the Smith-Watson-Topper [8] fatigue parameter
 12 is used to predict crack nucleation, following the methodology established by Sum et al. [29]
 13 and further developed in [18] for application to crack nucleation, via back-extrapolation of
 14 fatigue constants using linear elastic fracture mechanics to infer the lives corresponding to 10
 15 μm crack lengths, for example, for given stress levels. It was shown in [29] that the FE-
 16 implementation of this approach can capture stress gradient effects, e.g. the contact size effect;
 17 this is attributed to the built-in volume-averaging nature of the Gaussian sampling technique in
 18 the FE method. The critical plane approach is based on the physical observations that fatigue
 19 cracks initiate and grow within a material on certain planes, where the growth and orientation
 20 depends on the normal stresses and strains on these planes. The *SWT* life prediction equation
 21 employs a combined high-cycle fatigue (HCF) and low-cycle fatigue (LCF) equation, and
 22 consideration of the peak stress to account for the mean stress effect, as follows:

$$23 \quad SWT = \sigma_{\max} \frac{\Delta \varepsilon}{2} = \frac{\sigma_f'^2}{E} (2N_f)^{2d} + \sigma_f' \varepsilon_f' (2N_f)^{d+e} \quad (15)$$

24 where σ_{\max} is the peak normal stress on the critical plane, $\Delta \varepsilon$ is the maximum normal strain
 25 amplitude on the same plane, σ_f' and d are the (Basquin) fatigue strength coefficient and
 26 exponent (HCF constants), ε_f' and e are the (Coffin-Manson) fatigue ductility coefficient and
 27 exponent (LCF constants) and E is Young's modulus. The values of these constants
 28 corresponding to 10 μm crack nucleation employed here for Ti6Al4V, as obtained from [18]
 29 and [20] are listed in Table 4.

1 The FE-implementation of the critical-plane *SWT* parameter is achieved by transforming
 2 the time histories of element centroidal stresses and strain ranges onto planes at 5° intervals
 3 over a 180° range using the two-dimensional transformation (Mohr's circle) equations for
 4 stress and strain. The maximum normal stress σ_{\max} with respect to time, and the corresponding
 5 strain range $\Delta\varepsilon$ are determined for each of the 36 planes in each element. $\Delta\varepsilon$ is the difference
 6 between the maximum and minimum values of strain normal to the candidate plane over the
 7 complete loading cycle. Thus, *SWT* values are obtained for each candidate plane in each
 8 element. These values are then employed to establish the maximum critical plane *SWT* value
 9 with respect to plane orientation in each element, which in turn is used with Eq. (28) to furnish
 10 a number of cycles to failure, N_f .

11 One of the difficulties in the case of combined wear-fatigue calculations is the fact that
 12 the stress cycles change with evolving contact geometry. Thus, a fatigue damage accumulation
 13 methodology is required. The Miner-Palmgren rule is used here to calculate the damage
 14 accumulation, as follows:

$$15 \quad W = \sum_{i=1}^N \frac{n_i}{N_{fi}} \quad (16)$$

16 where n_i is the number of cycles experienced at loading cycle i with an associated *SWT* value
 17 of SWT_i and N_{fi} is the predicted number of cycles to failure (via Equation 15) for SWT_i . The
 18 occurrence of $W = 1$ indicates predicted location, orientation and number of cycles for crack
 19 nucleation.

21 *3.6 Ratchetting failure model*

22
 23 Following the approach developed by Leen and co-workers in [12], it is assumed here
 24 that for a ratchetting failure to occur, the total accumulated strain must reach a critical value ε_c ,
 25 which is defined as the stress-triaxiality dependant material ductility [30]. This value depends
 26 on the local stress triaxiality resulting from geometric constraints and loading condition. The
 27 number of cycles to failure by ratchetting N_r can be predicted using the following equations:

$$28 \quad \sum_i^{N_r} \Delta\varepsilon_r = \varepsilon_c \quad (17)$$

$$\Delta\varepsilon_r = \sqrt{\frac{2}{3}\Delta\varepsilon_{ij}^r\Delta\varepsilon_{ij}^r} \quad (18)$$

where $\Delta\varepsilon_r$ is a (uniaxial) equivalent ratchetting strain, corresponding to a multiaxial ratchetting strain condition. Hence there is a possible competition between failure due to (i) ductility exhaustion via ratchetting and (ii) fatigue failure (low- or high-cycle or combined) as represented here by the critical-plane SWT parameter. Thus, whichever occurs first, viz. ductility exhaustion or critical fatigue damage, determines the mechanism, location and life to crack nucleation.

8

9 *3.7 Tribological data*

10

11 A coefficient of friction (COF) μ value of 0.9 is used for the RF1 model, based on the
 12 experimental measurements from [20] from stabilised gross sliding tests. A COF value of 0.8 is
 13 used for both RF2 and RPF, based on the test data reported in [15].

14 The energy wear coefficient for the RF1 model has been identified from the test
 15 programme and data described in [20]. Specifically, following the method described in [13],
 16 the wear volume corresponding to different numbers of fretting cycles was plotted against
 17 accumulated energy, as represented in Equation 9 and the slope represents the energy wear
 18 coefficient, α . The resulting value for RF1 is $1.12 \times 10^{-8} \text{ MPa}^{-1}$. Furthermore, the formulation of
 19 the present paper has been compared with the previous Archard-based formulation from [20]
 20 for RF1 gross slip conditions and was shown to give identical results (in terms of wear scar
 21 depth profile evolution up to 100,000 cycles).

22 The fretting wear scars and hysteresis loops for the test corresponding to RF2 have been
 23 presented in detail in [15], permitting identification of the energy wear coefficient (α value)
 24 fore RF2 and RPF, as $7.121 \times 10^{-7} \text{ MPa}^{-1}$ ($7.121 \times 10^{-4} \text{ mm}^3/\text{J}$).

25

26 **4. Results and discussion**

27

28 *4.1 Validation of unworn FE modelling methodology*

29

1 The establishment of a satisfactory (converged) FE mesh is critical to the prediction of
2 accurate stresses, strains and hence plasticity and fatigue parameters in fretting problems. The
3 theoretical solutions for the Hertzian (frictionless) problem have been presented above and
4 these results are employed here to validate the FE model of the cylinder on flat fretting
5 geometry (called RF1 above). Figs. 10a and 10b show the comparisons of the FE-predicted
6 contact pressure and sub-surface stresses, along the Y (vertical)-axis, using the mesh of RF1
7 (Fig. 4), with the Hertzian (frictionless) solution from [21], for normal loading only. Clearly,
8 the FE model gives excellent agreement for the frictionless case. Fig. 10c shows a comparison
9 of the FE-predicted and theoretical frictional shear stress distribution (from [21]), under a
10 sliding tangential load combined with normal loading, at a depth of 20 μm along the horizontal
11 surface (parallel to the free surface of the flat specimen). The FE frictional solution is in
12 excellent agreement with the theoretical solution. The mesh for the USAF round on flat fretting
13 geometry, RF2 (see Fig. 5), gave the same quality of agreement with the theoretical solution.
14 The development of a theoretical solution for the nearly-complete problem of a rounded punch
15 on flat contact problem under combined normal and tangential loading is a more recent
16 development [5,6] and indeed, as highlighted above, the most recent solutions, as presented in
17 [6], are only applicable within certain geometrical limitations, specifically, $a \leq c \leq b$, viz. the
18 stick-zone semi-width must lie between the flat semi-width and the contact semi-width. This is
19 actually a narrow range of allowable geometries. The benefit of the FE modelling approach is
20 that it does not have such limitations, provided due account is taken of large deformation and
21 finite sliding effects. Another limitation of the findings presented in [6] is that no closed-form
22 solution for stress distributions was presented; only single point expressions for trailing edge
23 stress were presented. Clearly, the FE solution provides an approximate distribution of stress.
24 Figs. 11 to 14 show comparisons of key FE-predicted fretting and contact variables with the
25 corresponding theoretical results from [6] for the RPF model. A key challenge in the present
26 work is to develop a sufficiently refined mesh to capture the severe stress gradients associated
27 with the nearly-complete contact edges, on the one hand, and yet remain computationally
28 efficient in terms of minimising the run-times required for wear simulations over large
29 numbers of fretting cycles. Significant effort was therefore expended in the development of
30 such a suitable mesh (Fig. 6). Fig. 11 shows that the predicted contact pressure distribution

1 under normal loading for the final RPF mesh is in close agreement with the theoretical result;
2 for example, the maximum difference is 13% at the peak pressure location (edge of contact).
3 The slight discrepancy is attributed due to the FE mesh having necessarily employed a large
4 deformation assumption for accurate resolution of the contact tractions, whereas the theoretical
5 solution is based on a small deformation assumption. Fig. 12 shows a comparison of the FE
6 and theoretical predictions for contact semi-width across a range of normal loads, again
7 showing excellent agreement between the two methods, with the difference increasing with
8 increasing load and deformation. Under tangential loading $Q/\mu P = 0.5$ for the RPF model with
9 a COF (μ) of 0.8, a partial slip and a stick zone develop and a trailing-edge tensile stress peak
10 develops also, leading under cyclic tangential loading to fretting cracking. Therefore, the
11 accurate prediction of these trailing edge stresses is critical to fretting damage prediction. Fig.
12 13 shows a comparison of FE-predicted and theoretical stick zone semi-width, c , as a function
13 of pad geometry parameter a/b , illustrating convergence of the predicted results for large
14 values of a/b , viz. $a/b > 0.95$; again, the small deformation assumption appears to be
15 questionable for $a/b < 0.95$. Small a/b is associated with large load conditions (for example,
16 when $a/b = 0.8$, $P = 16253$ N/mm and $Q = 4063$ N/mm), and in these conditions the theory is
17 limited relative to the FE. (The theory assumes that: the strains are very small compared with
18 each body and the relative radii of curvature of the surface.) The a/b ratios of the present paper
19 are above 0.95. Fig. 14 shows a comparison of the FE-predicted distribution of tangential (σ_x)
20 stress with the theoretically-predicted trailing edge tensile stress peak (from Equation 1); the
21 FE model agrees with the latter to within 11%.

22

23 *4.2 Validation of FE energy-based wear simulation*

24

25 Having established successful performance of the unworn FE models for both the round
26 on flat and rounded punch on flat fretting configurations, the next logical step is to validate the
27 performance of the wear simulation methodology. One aspect of this validation is to examine
28 the performance of the energy-based wear simulation method against previous Archard-based
29 implementations, e.g. [20]; a second aspect is the compare the energy-based wear predictions
30 with measured test data. Fig. 15a shows the FE-predicted wear scar evolution in the RF1

1 cylinder on flat arrangement for the gross slip case of Table 2 for 100,000 cycles. These results
2 are almost identical to the Archard-based simulation results of [20]. The wear scar is predicted
3 to have a U-shape and the scar width and depth increase as the number of cycles increases. Fig.
4 15b shows the predicted evolution of contact pressure with fretting cycles, for the instant of
5 zero tangential displacement in each of the selected cycles up to 100,000 cycles. Clearly, the
6 contact pressure peak is predicted to drop dramatically within the first 24,000 cycles from more
7 than 400 MPa to about 100 MPa and thereafter decays more slowly. Concomitantly, the
8 pressure distribution becomes more uniform with increasing cycles. These results are
9 consistent with previously published gross slip wear simulation predictions [10, 20].

10 Figs. 16a and 16b show corresponding FE-predicted results for the partial slip case (Test
11 2 of Table 2) for the RF1 round on flat geometry. These results are consistent qualitatively with
12 the partial slip predictions of Mohd Tobi et al. [12], but those of [12] are closer to the
13 experiment values due to having matched the Archard wear coefficient directly to the
14 experimental data. The following key points can be noted from Figs 16a and 16b:

- 15 • the wear scar is predicted to increase in width with increasing cycles, but more slowly
16 than the gross slip case, and the stick zone is predicted to decrease in size, due to
17 plasticity at the stick-slip interface leading to increased slip and hence wear at this
18 interface.
- 19 • the contact pressure distribution is initially Hertzian with a peak at the centre of contact;
20 with wear, the contact pressure in the slip zones reduces gradually to an almost negligible
21 value, causing a pressure distribution more akin to that of a rounded punch on flat with
22 peak values of about 770 MPa at the stick zone edges after 300,000 cycles.

23
24 Figs. 17 and 18 show comparisons of the FE-predicted wear scars with measured 2D
25 profiles from the experimental wear scars, for the partial and gross slip tests of Table 2. Table 5
26 shows a tabulated comparison of some of the key data from these figures. The predicted scar
27 width is good for the gross slip case and although the maximum measured depth is about twice
28 the predicted value, the wear volumes look consistent and measurements effectively fluctuate
29 about the numerical prediction. For the partial slip case, the maximum wear depth is

1 significantly under-predicted by a factor of about 10 relative to the measured value although
2 the stick zone width and the scar width are in reasonably good agreement.

3 4 *4.3 Wear predictions for RF2 and RPF geometries*

5
6 The key objective of the present paper is to provide a comparative assessment of the
7 predicted fretting performance of two contrasting contact geometries under the same normal
8 load but across a range of applied displacements. Table 3 summarises the range of half-strokes
9 adopted for this comparative study. Note that the normal load employed is 208 N/mm, which is
10 a small fraction of the normal yield load for the RF2 geometry of 5536 N/mm; thus the RF2
11 tests are well within the elastic domain under normal loading. The FE analyses confirm that the
12 RPF normal load is also well within the elastic domain. Figs. 19 to 21 show sample results
13 from the predicted fretting wear behaviour of the RF2 and RPF geometries and Table 6
14 provides a quantitative comparison of the key wear scar data for both cases. Fig. 19 shows the
15 evolutions of the RF2 worn flat surface across the range of Δ values. Fig. 20 shows
16 corresponding evolutions for the RPF gross slip cases. Fig. 21a shows the evolution of contact
17 pressure for the RF2 14 μm half-stroke case, which shows a typical partial slip pressure
18 evolution profile as described before in Fig. 16b. Fig. 21b shows the dramatic effect of wear
19 under 14 μm half-stroke condition (note it is gross slip condition) for the RPF geometry, with
20 the edge-of-contact (EOC) peak pressures removed completely and a new more uniform
21 pressure distribution exhibiting certain features of the (worn) Hertzian type distribution with
22 localised peaks on the right hand side. It should be noted that with wear, particularly due to the
23 cycle jumping technique, whereby the material removal for ΔN cycle is applied incrementally
24 during the tangential loading cycle, it is inevitable that the instantaneous pressure distributions
25 for $N > 0$ will be non-symmetric. This is true for both the RF2 case, although less pronounced,
26 and more obviously the RPF case (Fig. 21b). Some other key points to be noted from these
27 results are as follows:

- 28 1. The FE predictions indicated no stabilised partial slip solution for the RPF, consistent
29 with the theoretical findings of [5], and therefore the wear simulation method predicted
30 no wear for these cases

2. As a result, the initial contact pressure profile is predicted to persist with two peaks at the EOC positions.
3. Due to the larger initial contact width, the predicted RPF (GS) wear scars are much more uniform than the RF2 scars.
4. The GSR threshold (Δ_{th}) is calculated to be 15 μm for the RF2 model and 12 μm for the RPF model.
5. Partial slip wear is predicted for the RF2 model but the reduction of applied displacement leads to a dramatic reduction in wear volume and wear scar dimensions; for example, reducing the half-stroke from 20 μm (GS) to 10 μm (PS), leads to a predicted reduction in maximum wear depth (after 25,000 cycles) of a factor of about 30. However, even in partial slip at 14 μm half-stroke, for RF2, a significant maximum (localised at stick-slip interface) wear depth of about 20 μm is predicted after 45,000 cycles. It is also worth to noting the prediction of extra deep wear pits at the stick-slip interface in Fig. 19 (b), due to the occurrence of localised plasticity, which is discussed in more detail in Section 4.4.
6. The predicted reduction in maximum scar depth with reducing half-stroke, from 20 μm (GS) to 14 μm (GS), for the RPF case is similar to that of RF2 (about 65% reduction), but of course there is a much more dramatic reduction to zero wear for RPF with further reduction in half-stroke below Δ_{th} , due to the transition to zero-slip or ‘stick’. Identification of Δ_{th} is therefore an important step in fretting wear characterisation, particularly for the rounded punch on flat fretting geometry and presumably also, by extension, for the general punch on flat fretting geometry.

4.4 Cyclic plasticity and ratchetting for RF2 and RPF geometries

It is shown in [12] for the same Ti6Al4V material as studied here, using a LKH materials model, that for partial slip, the cyclic plasticity effects lead, on the one hand, to ratchetting phenomena at the evolving stick-slip interface region, with associated plastic damage accumulation, which interacts with fatigue damage accumulation and, on the other hand, to accentuation of critical-plane *SWT* values predicting rapid crack nucleation, as observed

1 experimentally, and multiple cracking locations, as also observed experimentally. Although the
2 predictions in [12] demonstrated, for the first time, a wear-induced cyclic plasticity
3 phenomenon, whereby an ostensibly elastic initial (unworn) Hertzian contact problem is
4 predicted to develop significant cyclic plasticity and ratchetting behaviour at the evolving
5 stick-slip interface, the predicted accumulated plastic strains remained short of the ductility
6 exhaustion limit. The predicted ratchetting rate was observed to gradually decrease towards a
7 steady-state value of ratchet strain below the failure strain of the material. Thus it was not
8 possible, with the LKH model, to predict partial slip cracking due to ratchetting for these cases.
9 Hence, the present work has adopted a NLKH model which, as mentioned above, has been
10 shown to represent cyclic plasticity phenomena more realistically.

11 Figs. 22 and 23 present the results of the comparative contact geometry study in the
12 context of wear-induced plasticity. Firstly, no plasticity was predicted for the RPF geometry
13 and, secondly, only the 10 μm and 14 μm half-stroke RF2 cases gave plasticity. Figure 22a
14 shows that for the 14 μm case, which is very close to the Δ_{th} value of 12 μm for RF2, a
15 substantial and rapid accumulation of equivalent plastic strain (p) is predicted at the (evolving)
16 stick-slip interface, starting within the first 2000 cycles and reaching a peak accumulated value
17 of about 90% after 15,000 cycles at $x = -0.06$ mm. Fig. 22b shows the wear-induced evolution
18 of the individual plastic strain components at this location, demonstrating the development of
19 shear-driven plasticity at about 8000 cycles (at this location), leading to an almost uniform
20 ratchetting rate. As described in [12], this behaviour is dissimilar to conventional ratchetting,
21 where a constant cyclic load and hence stress/strain typically exists, in that it is primarily
22 driven by the predicted cyclically-increasing contact pressure at the stick-slip interface. Figs.
23 23a and 23b show a similar, but less detrimental, ratchetting behaviour for the 10 μm condition,
24 with lower overall resulting p (Fig. 23a) and a greater number of cycles before the onset of
25 plasticity.

26 27 *4.5 Critical-plane SWT evolution for RF2 and RPF geometries*

28
29 Figs. 24 to 26 illustrate some key detailed aspects of the critical-plane *SWT* crack
30 nucleation predictions from the round on flat (RF2) and rounded punch on flat (RPF) analyses.

1 Figs. 24a and 24b show the predicted wear-induced evolution of critical-plane *SWT* distribution
2 for 20 μm and 10 μm half-strokes in the round on flat; Figs. 24c and 24d show the
3 corresponding predictions for the rounded punch on flat. The results show that, in general, the
4 *SWT* levels in the rounded punch on flat are significantly lower than those in the round on flat.
5 For the round on flat, as presented previously, e.g. see [20], for similar geometries, material
6 removal due to wear is predicted to have a profound effect on the *SWT* distributions, leading to
7 an (i) attenuation (about 60%) and outward movement of peak *SWT* value (at EOC) with
8 increasing cycles for gross slip cases (Fig. 24a), due to stress re-distribution caused by wear
9 scar widening and (ii) accentuation (about 875%) and inward movement (towards the evolving
10 stick-slip interface) of peak *SWT* value with increasing cycles for partial slip cases (Fig. 24b).
11 These effects are compounded, in the present analyses, for the round on flat partial slip
12 condition, by cyclic plasticity phenomena. Thus a competitive relationship is predicted
13 between fatigue damage accumulation and ratchetting failure. The RPF initial peak *SWT* values
14 are only between about 18% (10 μm) and 7% (20 μm) of the corresponding RF2 values.
15 However, the wear-induced attenuation in peak *SWT* values is less significant for the RPF
16 cases, viz. between 0% (10 μm) and 20% (20 μm). It is worth noting that the initial (unworn)
17 critical-plane *SWT* value for the round on flat is about 50% higher for the 20 μm (GS) case
18 than for the 10 μm (PS) case, whereas for the rounded punch on flat the initial value of the 10
19 μm case is significantly higher than that of the 20 μm case. In other words, for the round on
20 flat, the initial fatigue parameter is higher for higher strokes, whereas for the rounded punch on
21 flat, it is higher for lower strokes. The former is a straightforward effect of increasing shear
22 traction with increasing PS stroke. However, for the RPF case, the transition from stick across
23 the contact to slip, leads to a redistribution of shear stress away from the localised peak value
24 at the leading EOC causing a small increase across a large portion of the contact width. Thus,
25 due to the very highly localised EOC stresses, when $\Delta < \Delta_{\text{th}}$ the predicted EOC slip is zero, so
26 that the peak localised EOC stress converts directly into a peak localised EOC *SWT* value (of
27 Figure 24d). In contrast, when $\Delta > \Delta_{\text{th}}$, the leading EOC shear stress peak is predicted to
28 significantly diminish, resulting in a 30% smaller predicted *SWT* peak for the 20 μm case than
29 for the 10 μm case.

1 Fig. 25a and 25b illustrate the predicted evolutions of critical-plane *SWT* at the identified
2 critical points along the contact surfaces of the round on flat, for the 20 μm and 10 μm half-
3 strokes. The RF2 20 μm *SWT* value is seen to reduce dramatically (from the initial high value)
4 within the first 5000 cycles for the region $|x| < 0.5$ and remains low thereafter, whereas the 10
5 μm value starts low but increases dramatically and remains high for longer in the region
6 $|x| < 0.25$. The RPF 20 μm *SWT* value follows a similar trend to the RF2 case but, as shown
7 in Figure 26a, results in a very similar but slightly higher steady-state value than the RF2. Fig.
8 26b shows a comparison of the *SWT* evolution for RF2 and RPF at 10 μm half-strokes; the
9 round on flat case is predicted to accrue significantly more fatigue damage over the first 60,000
10 cycles, even if the final steady-state values are somewhat similar.

11

12 4.6 Competition between ratchetting and fatigue

13

14 Table 7 presents a summary of the predicted numbers of cycles to 10 μm crack
15 nucleation, both with and without the assumption of wear-induced material removal effects
16 (since many studies still neglect wear effects in fatigue calculations) and also the predicted
17 numbers of cycles to first ratchetting-induced cracking. Fig. 27 shows a graphical comparison
18 of the effect of contact geometry and wear on predicted crack nucleation life as a function of
19 half-stroke. The graph clearly displays a minimum nucleation life for the round on flat (RF2)
20 when wear effects are incorporated, at 14 μm , which is very close to the Δ_{th} value of 15 μm .
21 (As discussed before in detail, e.g. see [16], these ‘with wear’ predictions are thus consistent
22 with the experimentally-observed trend of a minimum fatigue life, corresponding broadly to
23 the PS-GS threshold, as encapsulated also in the fretting maps of [2], whereas the ‘without
24 wear’ predictions are thus inconsistent with respect to this aspect). For the round on flat, wear
25 is predicted to have a significant detrimental effect of reducing life for $\Delta < \Delta_{\text{th}}$ (partial slip),
26 from the HCF to the LCF domain, but a contrasting beneficial effect of increasing (HCF) life
27 for $\Delta > \Delta_{\text{th}}$ (gross slip). The corresponding predictions for the rounded punch on flat are
28 significantly different from these. Firstly, the predicted effect of wear is significantly less, the
29 only noticeable effect being a predicted beneficial increase in (HCF) life for the $\Delta = 14 \mu\text{m}$
30 case (gross slip), from 4.6×10^{11} cycles to 2.4×10^{13} ; interestingly, for the $\Delta = 20 \mu\text{m}$ case, the

1 EOC peaks are predicted to wear so fast that negligible fatigue damage accrues whereas, for
2 the 10 μm case, there is no predicted effect of wear because no slip or wear occurs. Secondly,
3 the effect of increasing stroke for the RPF is to increase life due to predicted decrease in EOC
4 *SWT* value, whereas increasing stroke is predicted to decrease life for RF2 while $\Delta < \Delta_{\text{th}}$, and
5 remain constant for $\Delta > \Delta_{\text{th}}$, consistent with previous ‘no wear’ predictions from [16], due to
6 the increasing shear traction with increasing stroke for $\Delta < \Delta_{\text{th}}$, reaching saturation at Δ_{th} .
7 Thirdly, the predicted RPF lives are significantly longer (all very high cycle fatigue), in general,
8 than the predicted RF2 lives. The one exception is the large stroke $\Delta = 20 \mu\text{m}$ case, where the
9 ‘with wear’ predictions indicate that a slightly shorter RPF life, 3.0×10^{12} cycles, compared to
10 2.2×10^{13} cycles.

11 Ratchetting failure is predicted to occur in the round on flat case for partial slip but not
12 for gross slip, whereas no plasticity or ratchetting failure is predicted to occur in the rounded
13 punch on flat. The numbers of cycles to predicted ratchetting failure are found to be
14 competitive with those to fatigue crack nucleation. For the RF2 partial slip cases, consistent
15 with previous work [20], crack nucleation is predicted at numerous locations across the slip
16 zone. For $\Delta = 14 \mu\text{m}$, fatigue crack nucleation is predicted first at $x = -0.10 \text{ mm}$ after
17 approximately 7000 cycles and next at $x = -0.06 \text{ mm}$ after approximately 9000 cycles, with
18 ratchetting failure predicted at $x = -0.06 \text{ mm}$ at 10,000 cycles, assuming a monotonic critical
19 value ϵ_c for Ti6Al4V of 12%. For $\Delta = 10 \mu\text{m}$, although first crack nucleation is predicted at $x =$
20 -0.12 mm after 34,000 cycles, ratchetting failure is predicted after approximately 48,000 cycles
21 at $x = -0.06 \text{ mm}$, just before predicted crack nucleation at that same location, at 49,000 cycles.
22 Thus, from the present analyses, wear-induced ratchetting failure is predicted to be highly
23 competitive with wear-induced fatigue crack nucleation for the round on flat under partial slip
24 conditions.

25 It is important to note that although the comparison with a sample measured PS wear
26 profile for RF1 suggests that the PS wear depth may be under-predicted by the energy-based
27 wear approach, it is anticipated that improved wear depth correlation with test data would
28 result in similar GS-PS trends for the RF1 and RF2 cases, except with lower predicted PS
29 fatigue nucleation life.

30

1 **5. Conclusions**

2 A finite element based energy wear simulation method has been implemented for
3 Ti6Al4V material. The method has been combined with (i) a critical-plane multiaxial fatigue
4 prediction method for crack nucleation using the *SWT* fatigue parameter and (ii) non-linear
5 kinematic hardening model for cyclic plasticity. Detailed FE models of two round on flat
6 fretting configurations and a rounded punch on flat geometry have been developed for a
7 comparative investigation on the effect of contact geometry on fretting wear, fatigue and cyclic
8 plasticity (ratchetting) performance for a given normal load and space envelop and across a
9 range of applied strokes. Validation against theoretical solutions for the round on flat and
10 rounded punch on flat have shown the developed FE models to be in excellent agreement with
11 the theoretical predictions of contact tractions and salient sub-surface stresses. Validation of
12 the round on flat wear prediction against previously published test results for partial slip and
13 gross slip have shown (i) that the gross slip predictions are in reasonable agreement with the
14 sample measured profile, and (ii) that the partial slip predicted stick-zone and contact widths
15 are in reasonable agreement but the partial slip predicted wear depth is about 10 times less than
16 the measured value. Identification of the wear and friction coefficient for the comparison study
17 was effected via previously published work from the literature for the second round on flat
18 geometry.

19 In terms of wear behaviour for the two fretting geometries, the following conclusions
20 result:

- 21 • A significant predicted difference is that the round on flat geometry can sustain a
22 stabilised partial slip solution with an associated wear pattern whereas the
23 rounded punch on flat (incomplete) geometry is predicted to stick, resulting in no
24 predicted wear, below the GSR threshold. The GSR threshold stroke is therefore
25 shown to be a significant parameter for designing against wear in nearly complete
26 contacts.
- 27 • Above the GSR threshold, the predicted wear scars in the rounded punch on flat
28 is of uniform depth whereas the round on flat scar is more U-shaped, of larger
29 maximum depth.
- 30 • The wear volume is larger for the rounded punch, particularly for the 14 μm case.

1 In terms of crack nucleation behaviour:

- 2 • The performances of the two geometries are significantly different, driven at least
3 partly by the significantly lower stresses and initial fatigue damage parameter
4 levels in the rounded punch case, despite the very localized edge of contact peaks.
5 Specifically, in general, the rounded punch was predicted to have a significantly
6 longer life to 10 μm crack nucleation (effectively infinite life), with the round on
7 flat typically in the HCF regime (typically mega-cycle).
- 8 • The predicted effect of slip regime and associated wear on fatigue crack
9 nucleation was much more significant for the round on flat than for the rounded
10 punch; for the former, the predicted effect of wear was to (i) reduce the partial
11 slip life from HCF to LCF and (ii) increase the gross slip life from HCF (mega-
12 cycles) to very high cycle fatigue. For the rounded punch, the predicted effect
13 was to slightly increase the life to nucleation (in the very high cycle regime) so
14 that for 20 μm , life was predicted to be less than the round on flat value.
- 15 • There was a difference in predicted effect of stroke on fatigue for round on flat
16 and for rounded punch. For the no-wear assumption, the predicted effect of
17 increasing stroke in the round on flat was to reduce life whereas the predicted
18 effect in rounded punch on flat was to increase life, due to the greater sensitivity
19 of the rounded punch *SWT* value to relative movement as a result of the more
20 localized edge of contact peak.
- 21 • For the round on flat, a significant effect of wear-induced cyclic plasticity was
22 predicted in the partial slip regime, whereby ratchetting failure was predicted to
23 occur within a similar number of cycles and at similar contact locations (stick-slip
24 interfaces) to fatigue crack nucleation. Thus, it is proposed that many partial slip
25 failures may be caused by wear-induced ratchetting, in addition to fatigue
26 cracking. No ratchetting was predicted for the rounded punch or for the gross slip
27 regime. The GSR threshold stroke was shown to be a significant parameter.

28 The presented findings have implications for the design of pressure armor layers in
29 flexible risers and other complex contact geometries, as follows:

- 1 • The importance of modeling and predicting wear, especially for Hertzian contacts in
2 partial and gross slip; not accounting for the effects of wear on stresses and fatigue
3 damage can be non-conservative in the PSR and over-conservative in the GSR
- 4 • The importance of identification of slip regime for nearly complete geometries; for
5 $\Delta < \Delta_{th}$, there is no need to model wear, whereas for the GSR, not modeling wear may
6 lead to over-conservative lives.
- 7 • If there is freedom to choose the contact geometry, for a specified normal load, space
8 envelop and known stroke, the nearly complete geometry is predicted to be superior in
9 terms of fatigue life, provided the radius to nominal geometry ratio is akin to that used
10 here; the nearly complete contact should give a significantly longer life, particularly in
11 partial slip. On the other hand, the round on flat is predicted to be superior in terms of
12 wear performance, particularly below the GSR threshold.

15 Acknowledgements

16 The authors wish to thank Dr. J. Ding (ITP Aeroengines, Alstom, UK) and A.L. Mohd
17 Tobi (University of Nottingham), for their helpful discussions.

20 References

- 22 [1] Hannel S, Fouvry S, Kapsa P, Vincent L. The fretting sliding transition as a criterion for
23 electrical contact performance. *Wear* 2001 Sep;249(9):761-770.
- 24 [2] Vingsbo O, Soderberg S. On fretting maps. *Wear* 1988 Sep;126(2):131-147.
- 25 [3] Cattaneo C, Sul contatto di due corpi elastici: distribuzione locale degli sforzi, *Reconditi dell*
26 *Accademia nazionale dei Lincei* 27 (1938), 342-348, 434-436, 474-478.
- 27 [4] Mindlin R.D., Compliance of elastic bodies in contact, *Journal of Applied Mechanics-*
28 *Transactions of the ASME*, 16 (3) (1949) 259-268.
- 29 [5] Ciavarella M, Hills D.A, Monno G., The influence of rounded edges on indentation by flat
30 punch, *Proceedings of the Institution of Mechanical Engineers Part C-Journal of Mechanical*
31 *Engineering Science* 212 (4) (1998) 319-328.

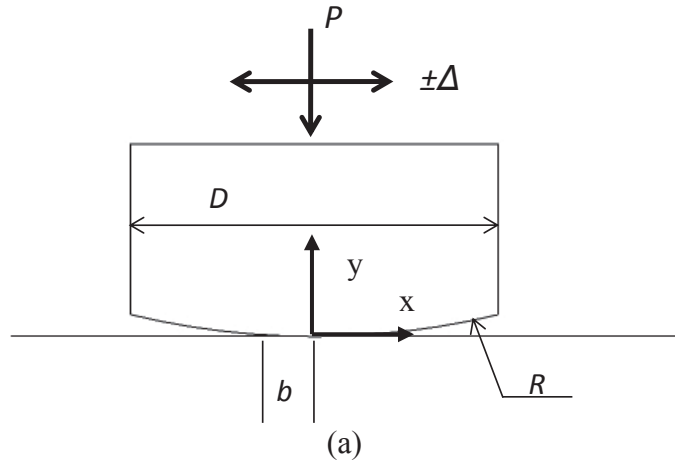
- 1 [6] Ciavarella M, Macina G, New results for the fretting-induced stress concentration on
2 Hertzian and flat rounded contacts, *International Journal of Mechanical Sciences*, 45 (3) (2003)
3 449-467.
- 4 [7] Szolwinski MP, Farris TN. Mechanics of fretting fatigue crack formation. *Wear* 1996
5 Oct;198(1-2):93-107.
- 6 [8] Smith KN, Watson P, Topper TH. A stress-strain function for the fatigue of metals. *J*
7 *Mater*, (1970) 15, 767-78.
- 8 [9] Archard JF. Contact and rubbing of flat surfaces. *J Appl Phys* 1953; 24: 981-8.
- 9 [10] McColl, I.R., Ding, J. & Leen, S.B. Finite element simulation and experimental validation
10 of fretting wear. *Wear* 256, 1114-1127 (2004).
- 11 [11] Ding, J., Leen, S.B. & McColl, I.R. The effect of slip regime on fretting wear-induced
12 stress evolution. *International Journal of Fatigue* 26, 521-531 (2004).
- 13 [12] Mohd Tobi, A., Ding, J., Bandak, G., Leen, S. & Shipway, P. A study on the interaction
14 between fretting wear and cyclic plasticity for Ti-6Al-4V. *Wear* 267, 270-282 (2009).
- 15 [13] Fouvry, S., Liskiewicz, T., Kapsa, P., Hannel, S. & Sauger, E. An energy description of
16 wear mechanisms and its applications to oscillating sliding contacts. *Wear* 255, 287-298
- 17 [14] Fridrici, V., Fouvry, S. & Kapsa, P. Effect of shot peening on the fretting wear of Ti-6Al-
18 4V. *Wear* 250, 642-649 (2001).
- 19 [15] Magaziner, R., Jain, V. & Mall, S. Wear characterization of Ti-6Al-4V under fretting-
20 reciprocating sliding conditions. *Wear* 264, 1002-1014 (2008).
- 21 [16] Madge, J., Leen, S., McColl, I. & Shipway, P. Contact-evolution based prediction of
22 fretting fatigue life: Effect of slip amplitude. *Wear* 262, 1159-1170 (2007).
- 23 [17] Madge, J., Leen, S. & Shipway, P. The critical role of fretting wear in the analysis of
24 fretting fatigue. *Wear* 263, 542-551 (2007).
- 25 [18] Madge, J., Leen, S. & Shipway, P. A combined wear and crack nucleation-propagation
26 methodology for fretting fatigue prediction. *International Journal of Fatigue* 30, 1509-1528
27 (2008).
- 28 [19] Feret, J.J. & Bournazel, C.L. Calculation of Stresses and Slip in Structural Layers of
29 Unbonded Flexible Pipes. *J. Offshore Mech. Arct. Eng.* 109, 263-269 (1987).
- 30 [20] Ding, J., Bandak, G., Leen, S., Williams, E. & Shipway, P. Experimental characterisation
31 and numerical simulation of contact evolution effect on fretting crack nucleation for Ti-6Al-

- 1 4V. Tribology International 42, 1651-1662 (2009).
- 2 [21] K. L. Johnson, Contact Mechanics, Cambridge University Press, Cambridge, 1985.
- 3 [22] Smith JO, Liu CK. Stresses due to tangential and normal loads on an elastic solid. Trans
4 ASME, Series E, J Appl Mech (1953); 20: 157-66.
- 5 [23] Sackfield A, Hills DA. Some useful results in the classical Hertz contact problem. J Strain
6 Anal Eng Des 1983; 18 (2): 101
- 7 [24] Jäger, J. New analytical and numerical results for two-dimensional contact profiles.
8 International Journal of Solids and Structures 39, 959-972 (2002).
- 9 [25] ABAQUS user's and theory manuals, Version 6.9. RI, US: HKS Inc.; 1998.
- 10 [26] Lemaitre, J. and Chaboche, J.L. (1990) Mechanics of Solid Materials.: Cambridge
11 University Press, Cambridge.
- 12 [27] Benedetti, M. & Fontanari, V. The effect of bi-modal and lamellar microstructures of Ti-
13 6Al-4V on the behaviour of fatigue cracks emanating from edge-notches. Fatigue & Fracture
14 of Engineering Materials & Structures 27, 1073-1089 (2004).
- 15 [28] Jin, O. & Mall, S. Influence of contact configuration on fretting fatigue behavior of Ti-
16 6Al-4V under independent pad displacement condition. International Journal of Fatigue 24,
17 1243-1253 (2002).
- 18 [29] Sum, W.S., Williams, E.J. & Leen, S.B. Finite element, critical-plane, fatigue life
19 prediction of simple and complex contact configurations. International Journal of Fatigue 27,
20 403-416 (2005).
- 21 [30] W.Y. Yan, E.P. Busso, N.P. O'Dowd, A micromechanics investigation of sliding wear in
22 coated components, Proceedings of the Royal Society of London A 456 (2000) 2387 - 2407.
- 23

Figure

1 Figures

2
3



4
5
6
7
8
9

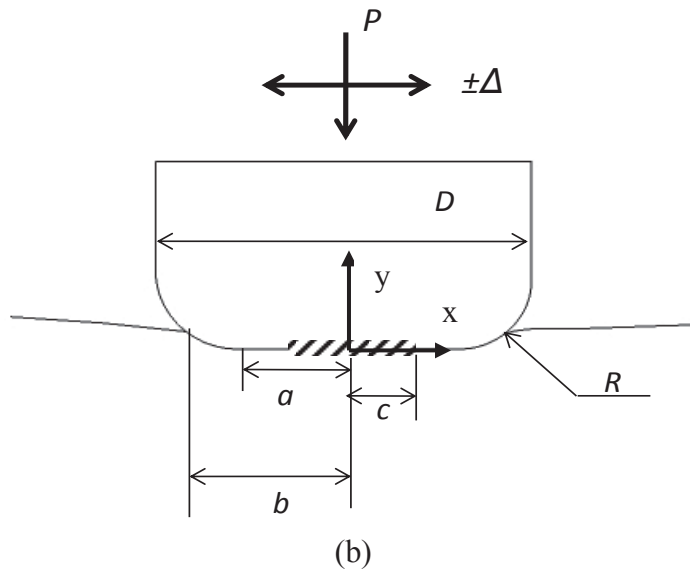


Fig. 1. Schematic of fretting contacts: (a) Round on flat (RF2)(Round radius $R = 50.8 \text{ mm}$, $D = 9.5 \text{ mm}$, half contact width b) and (b) Round punch on flat (RPF) (Radius $R = 2.54 \text{ mm}$, half flat region width $a = 2.25 \text{ mm}$, $D = 9.5 \text{ mm}$, half contact width b).

10
11

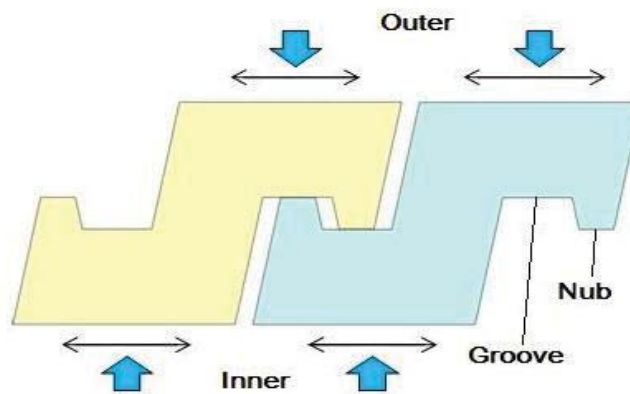


Fig. 2. Schematic of pressure armour layer contact.

1

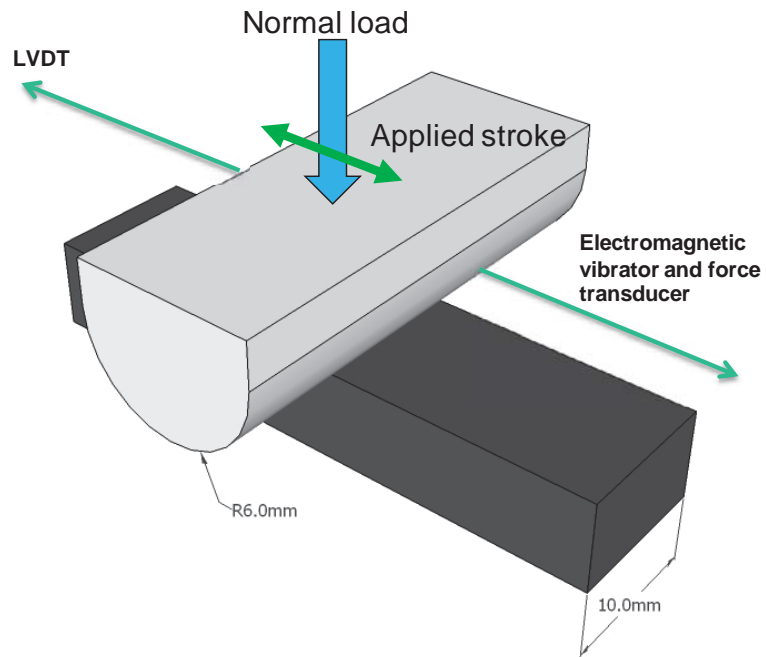


Fig. 3. Schematic of fretting test rig for RF1 test 1 and 2.

2
3
4
5
6
7

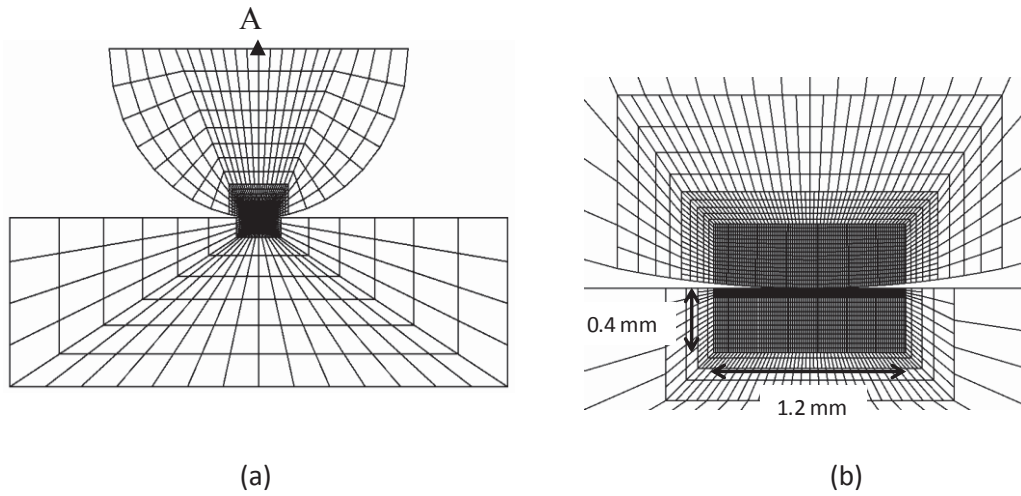


Fig. 4. Mesh details of FE model RF1 (a) full model, (b) contact region detail.

8
9
10
11
12
13

1
2

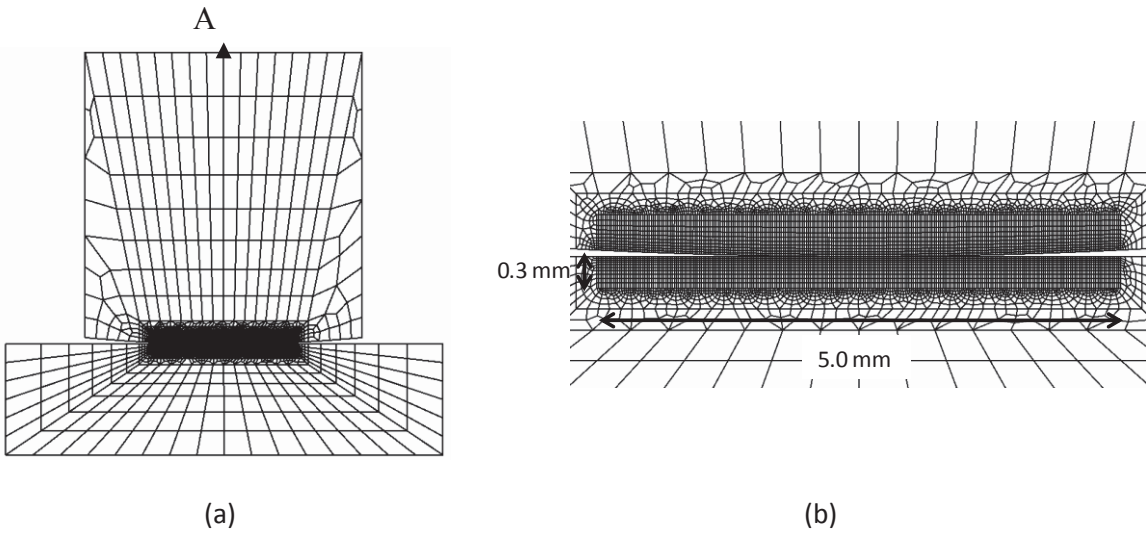


Fig. 5. Mesh details of FE model RF2 (a) full model. (b) contact region detail.

3
4
5

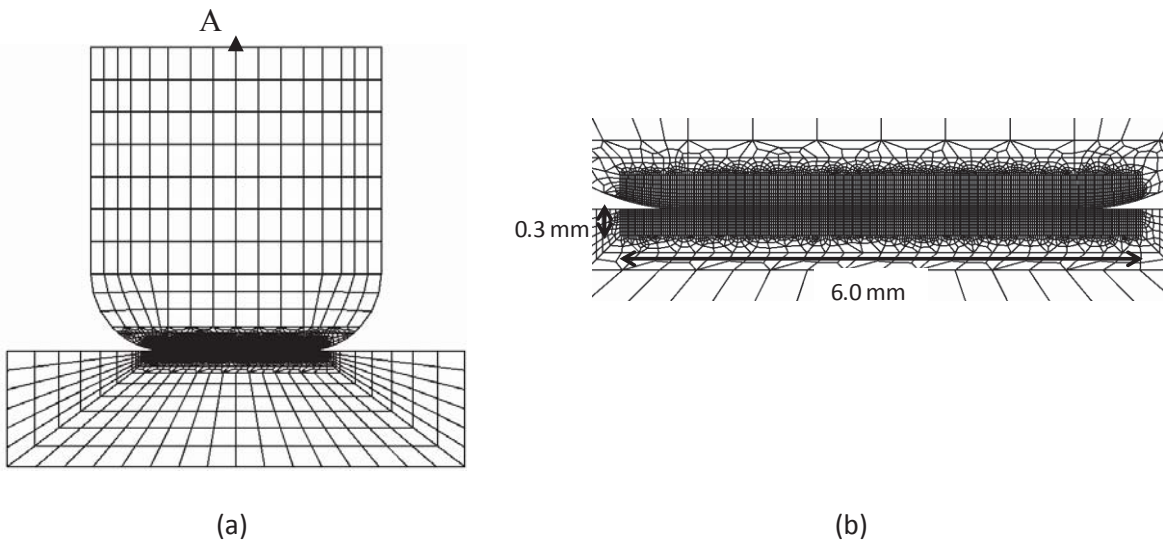
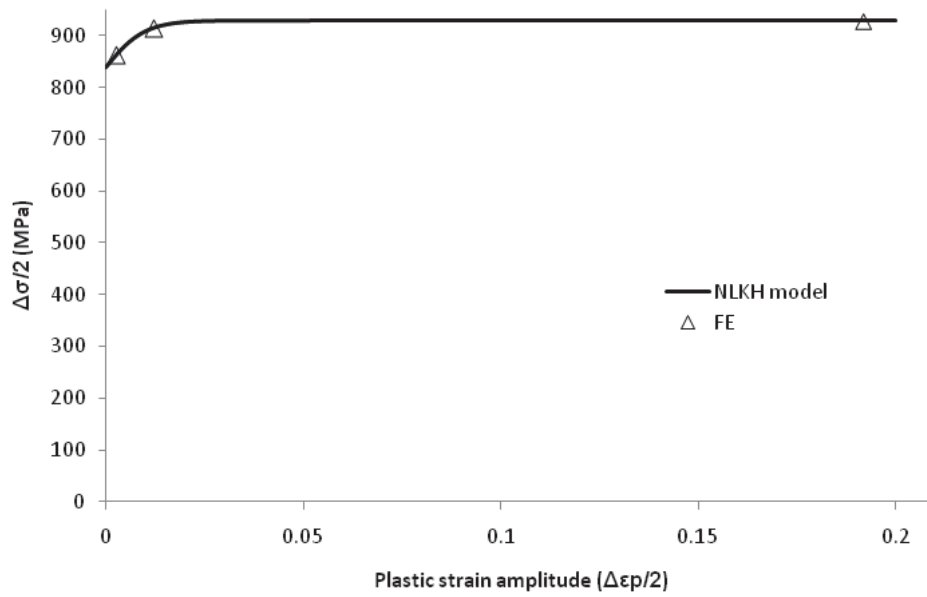


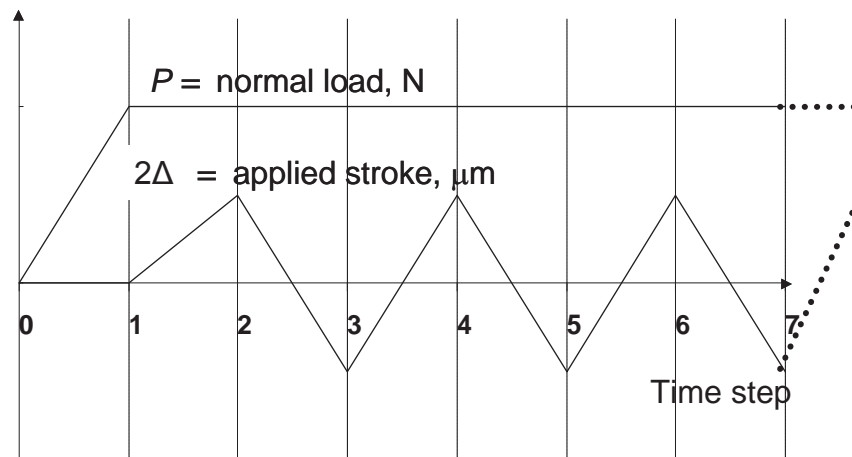
Fig. 6. Mesh details of FE model RPF (a) full model. (b) contact region detail.

6
7



1
2
3

Fig. 7. Comparison of FE-predicted cyclic behaviour with NLKH theoretical formulation.



4
5

Fig. 8. Displacement and load history for fretting experiments and analyses.

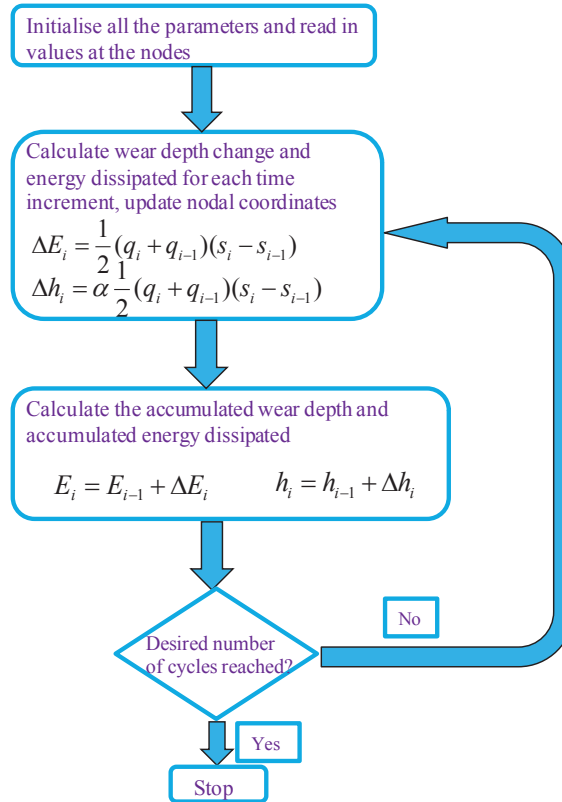
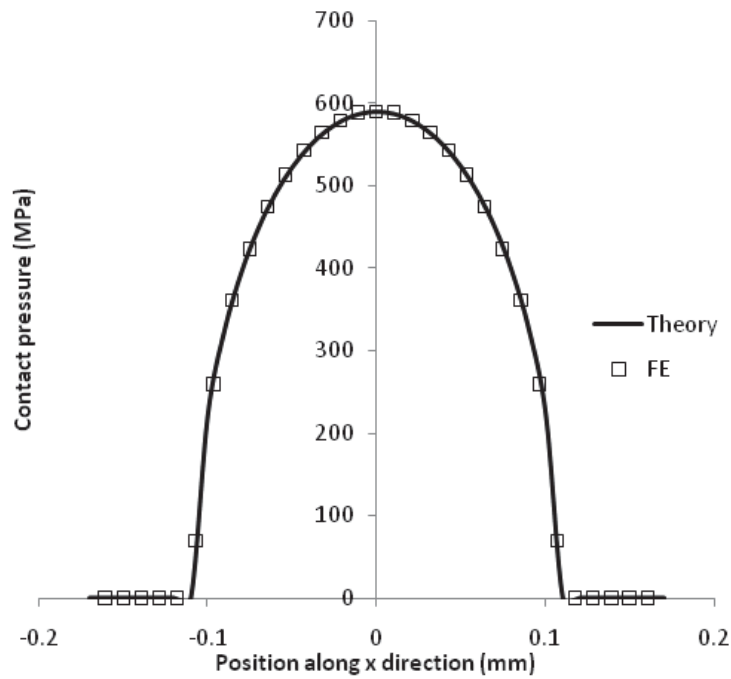
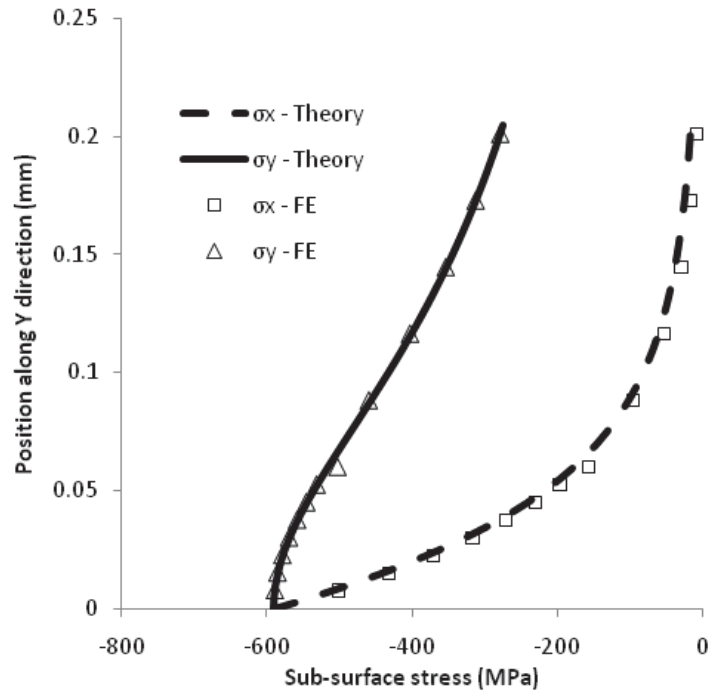


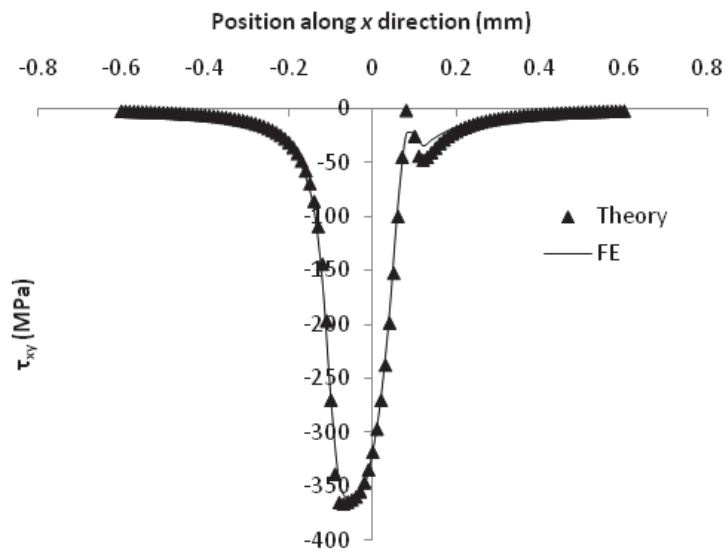
Fig. 9. Flowchart depicting FE implementation of energy wear methodology.



(a)

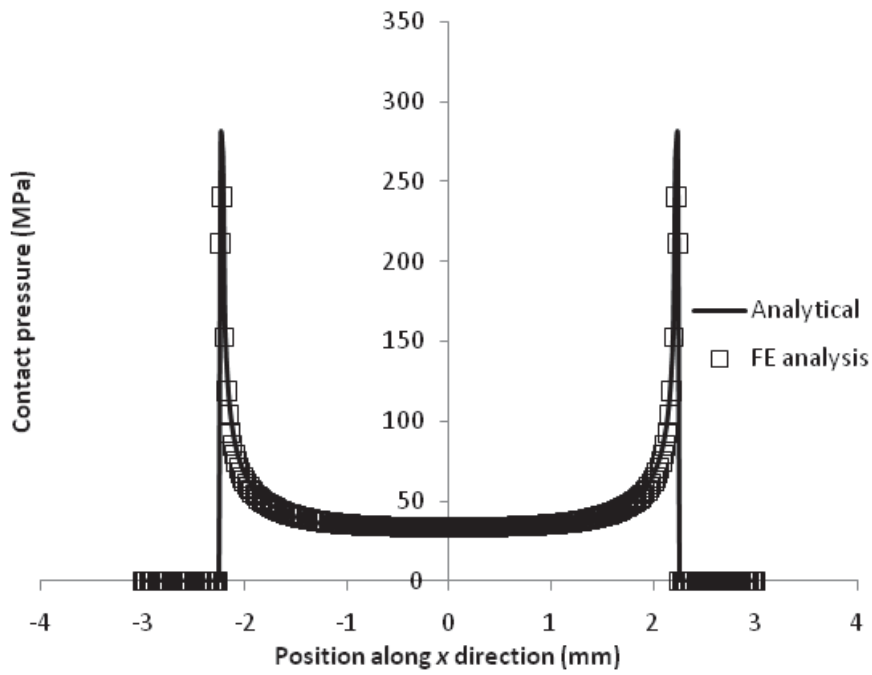


(b)

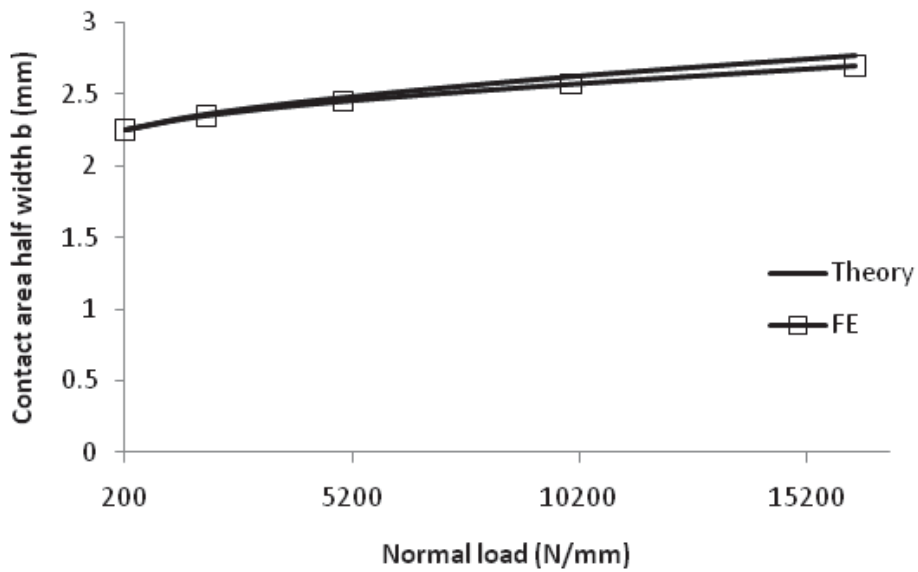


(c)

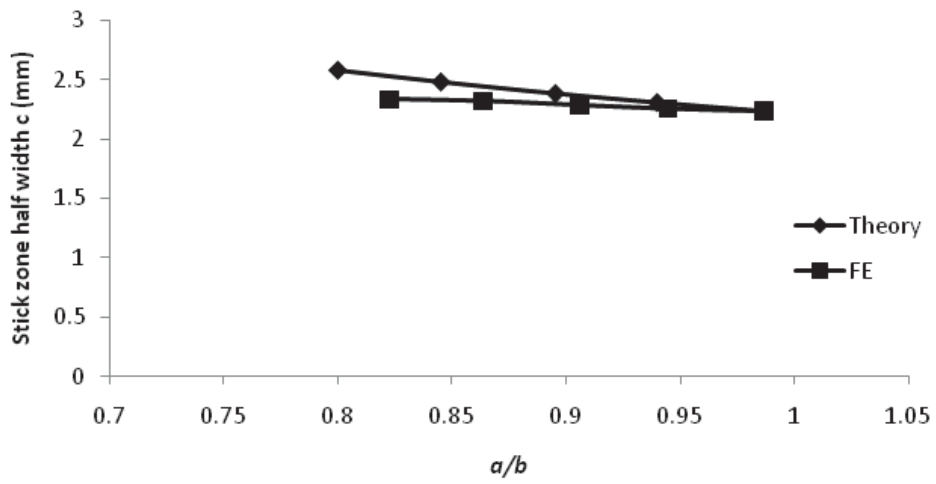
Fig. 10. Comparisons of RF1 FE prediction and analytical solution under a normal load of 100 N/mm: (a) distribution of contact pressure; (b) sub-surface stress along Y-axis; and (c) Distribution of shear stress τ_{xy} at depth $y = 20 \mu\text{m}$ for combined normal and tangential loading ($\mu = 0.6$).



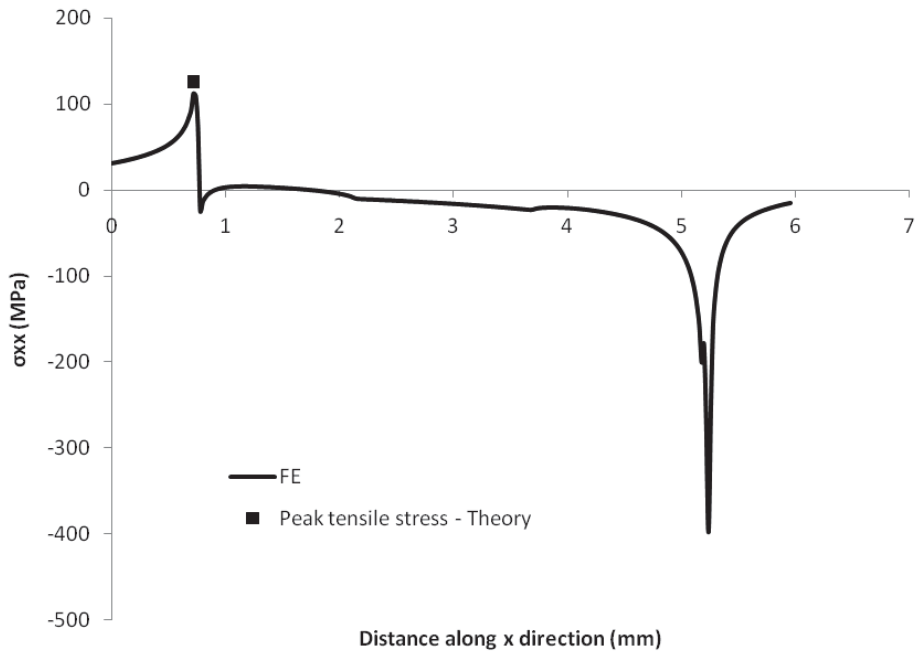
1
2
3
4
Fig. 11. Comparison of distribution of contact pressure between FE prediction and analytical solution, for RPF under a normal load of 208 N/mm.



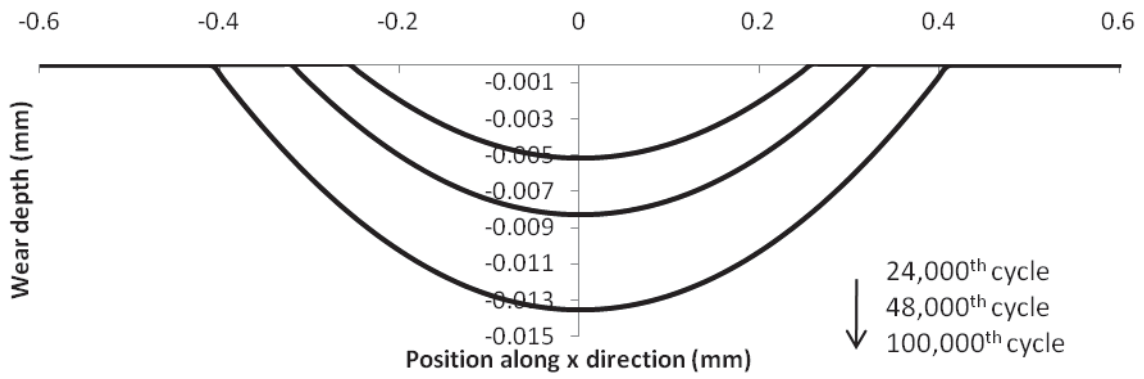
5
6
7
8
Fig. 12. Comparison of contact area half width between FE prediction and analytical solution, across a range of normal loads for RPF.



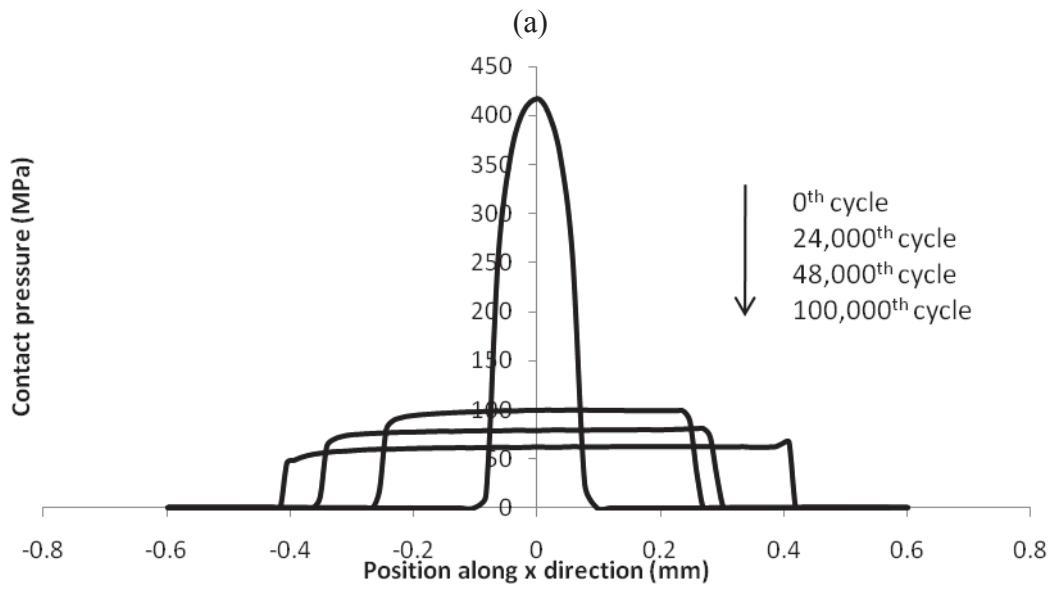
1
 2 Fig. 13. Comparison of stick zone half width between FE prediction and analytical solution, for RPF, across a
 3 range of a/b values, under $Q/\mu P = 0.5$ for RPF.
 4



5

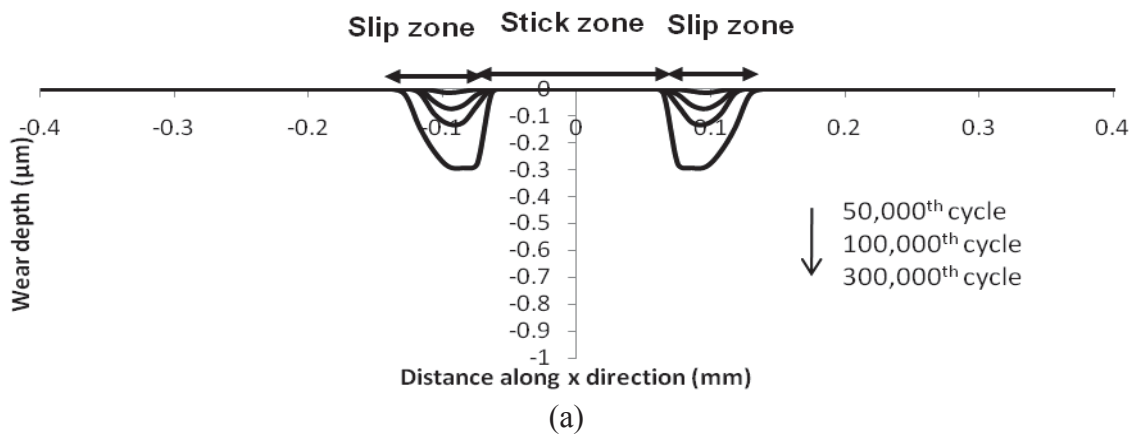


1
2

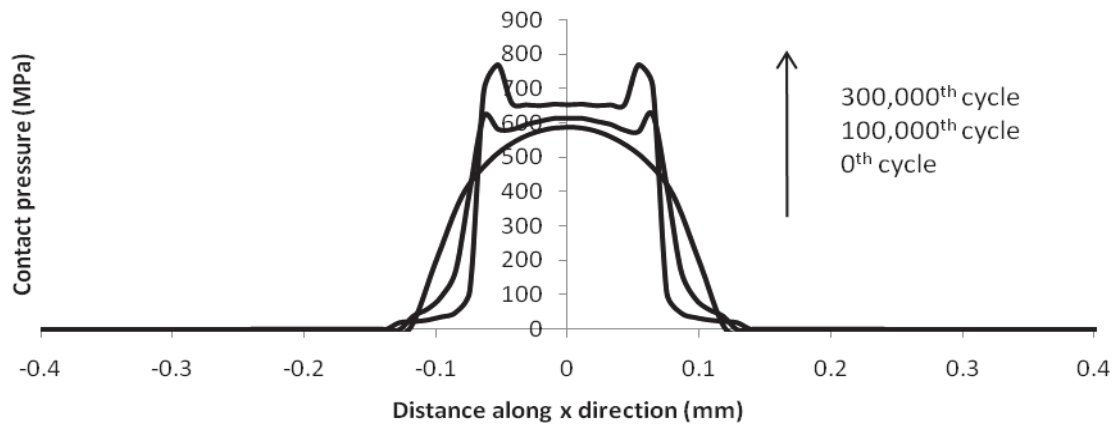


3
4
5
6

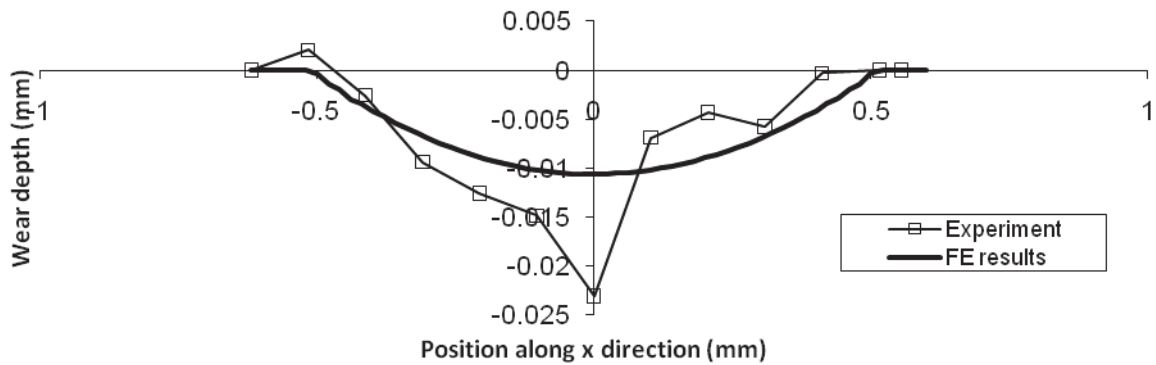
Fig. 15. Predicted evolutions of (a) wear profile and (b) contact pressure distribution for Test 1, RF1 GS .



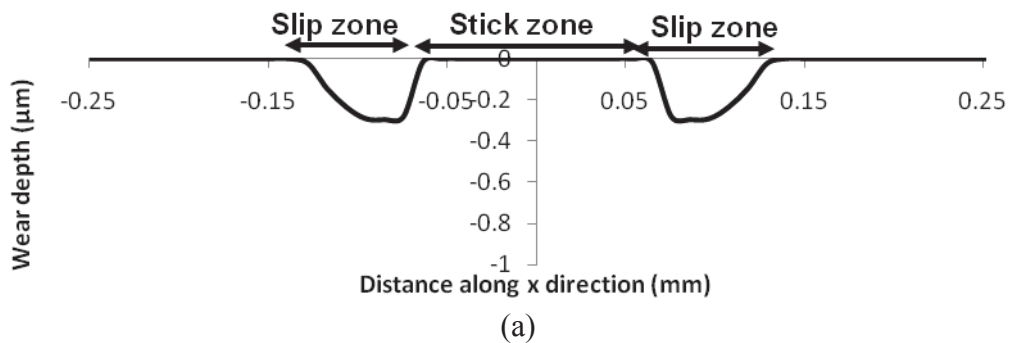
7
8



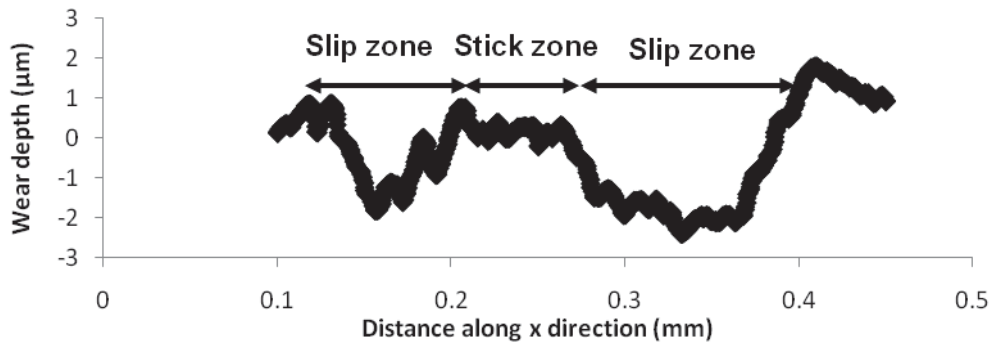
1
2
3 Fig. 16. Predicted evolutions of (a) wear profile and (b) contact pressure distribution for Test 2, RF1 PS.
4



5
6 Fig. 17. Wear scar comparison between FE (100,000 cycles) and experiment (100,000 cycles) for gross slip case
7 for RF1 Test 1.

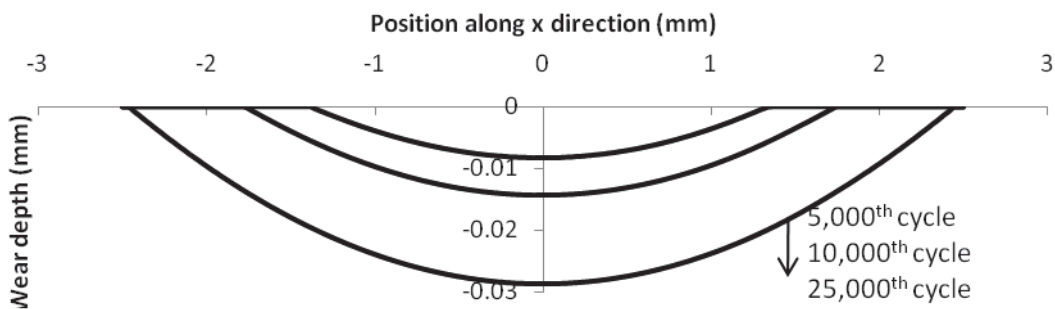


8
9

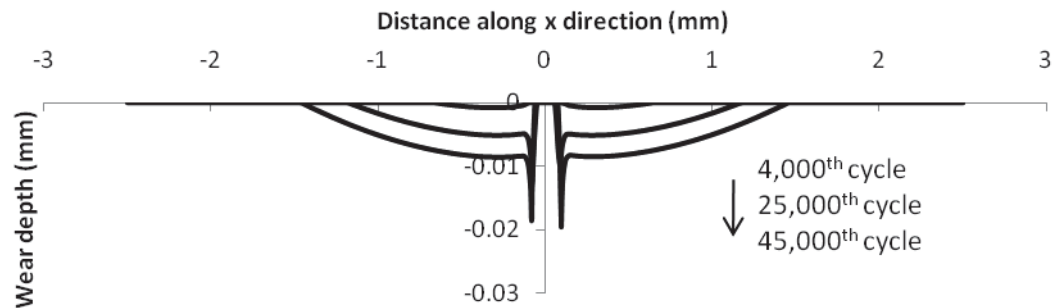


(b)

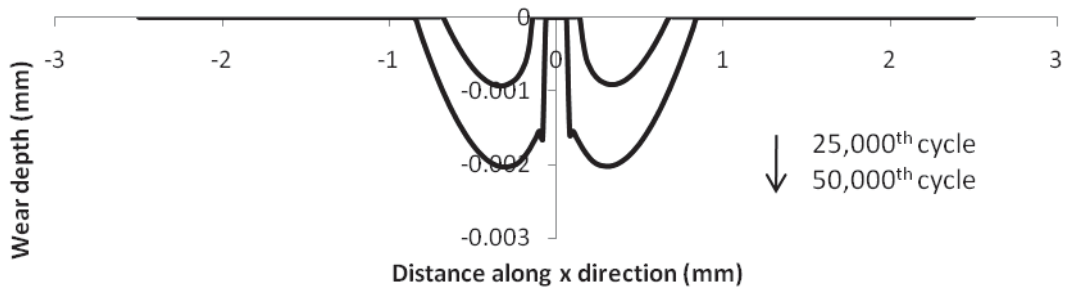
Fig. 18. Qualitative wear scar comparison between (a) FE (300,000 cycles) and (b) experiment (300,000 cycles) for partial slip case for RF1 Test 2.



(a)



(b)



(c)

1
2
3
4
5

6
7

8
9

10
11

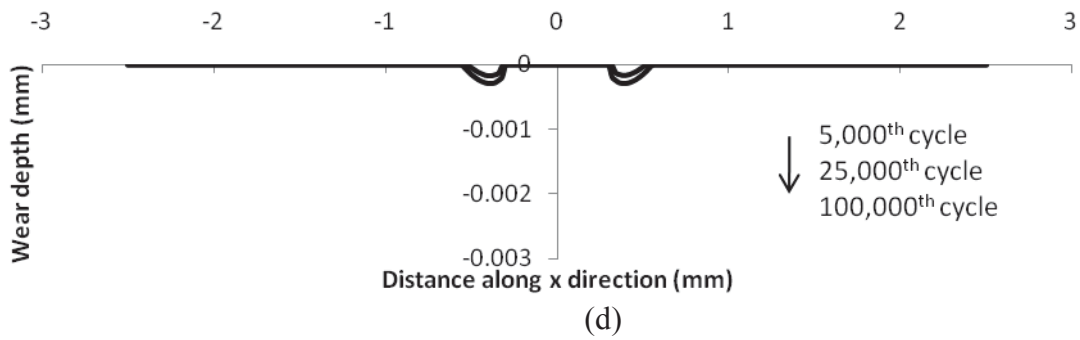


Fig. 19. Predicted evolutions of wear profile for RF2 : (a) 20 μm half-stroke, Analysis 6, (b) 14 μm half-stroke, Analysis 5, (c) 10 μm half-stroke, Analysis 4, (d) 7 μm half-stroke, Analysis 3.

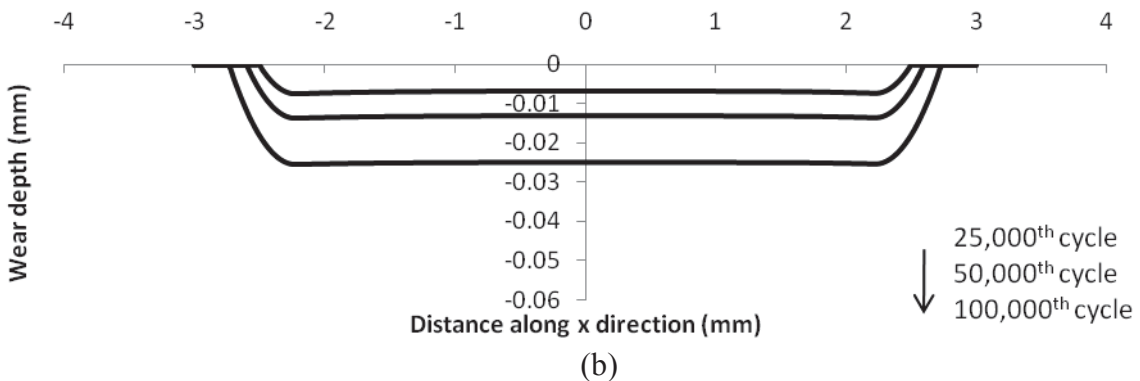
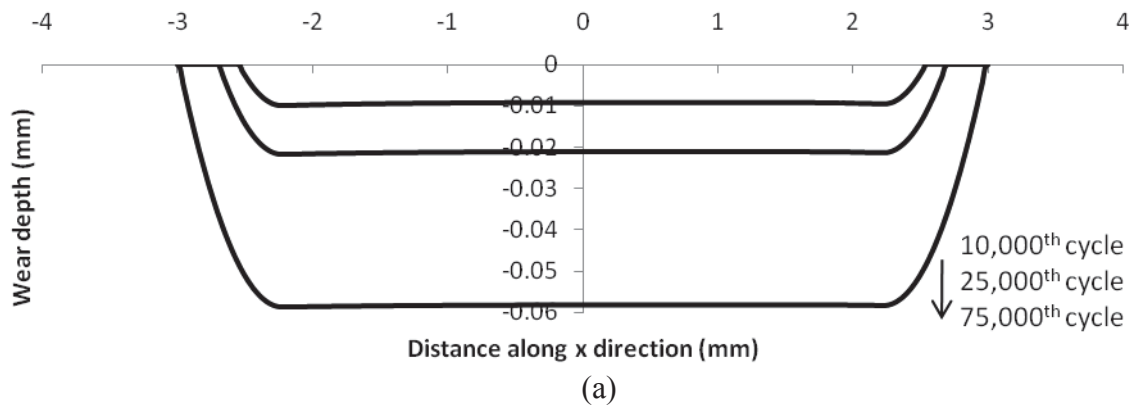
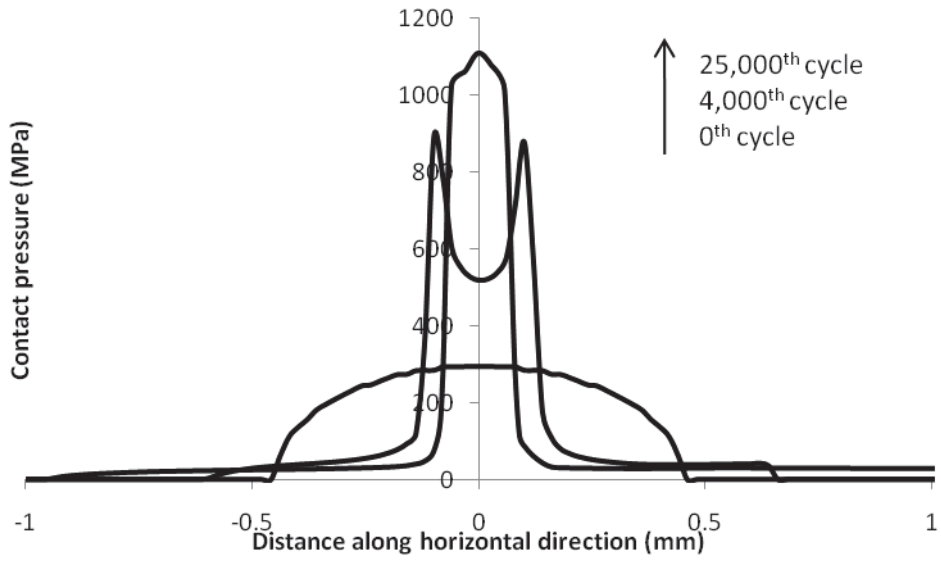
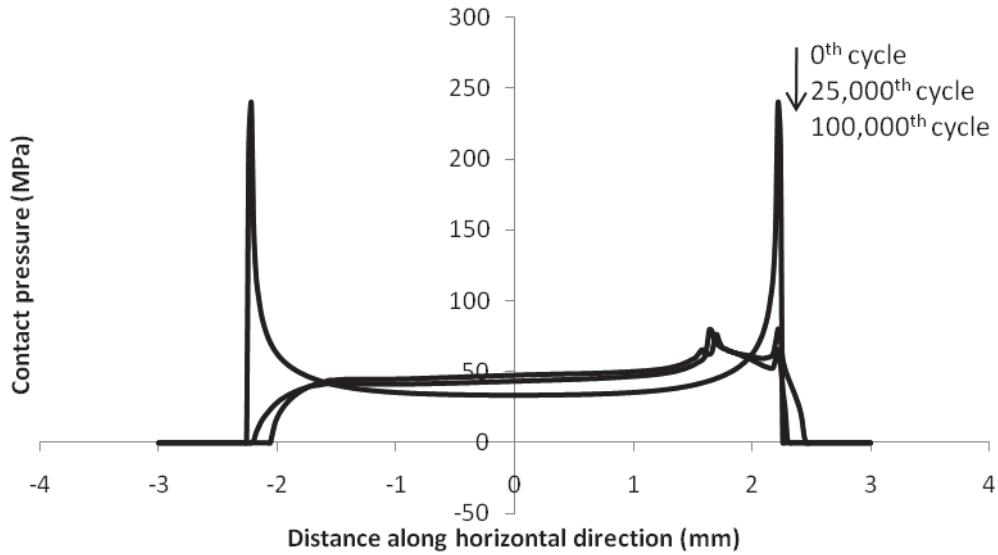


Fig. 20. Predicted evolutions of wear profile for RPF : (a) 20 μm half-stroke, Analysis 10, (b) 14 μm half-stroke, Analysis 9.



(a) Contact pressure evolution for RF2, 14 μm half-stroke.

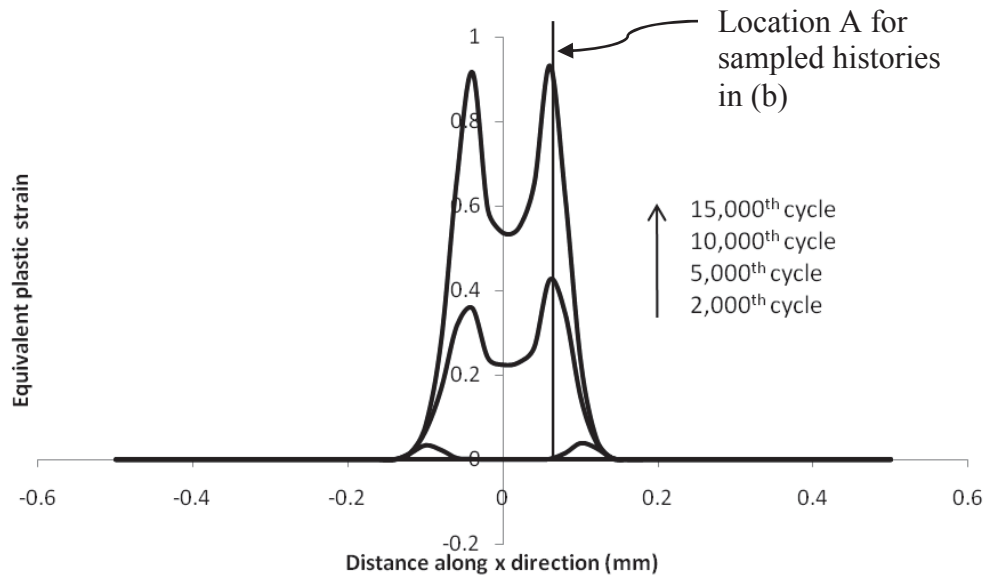


(b) Contact pressure evolution for RPF, 14 μm half-stroke.

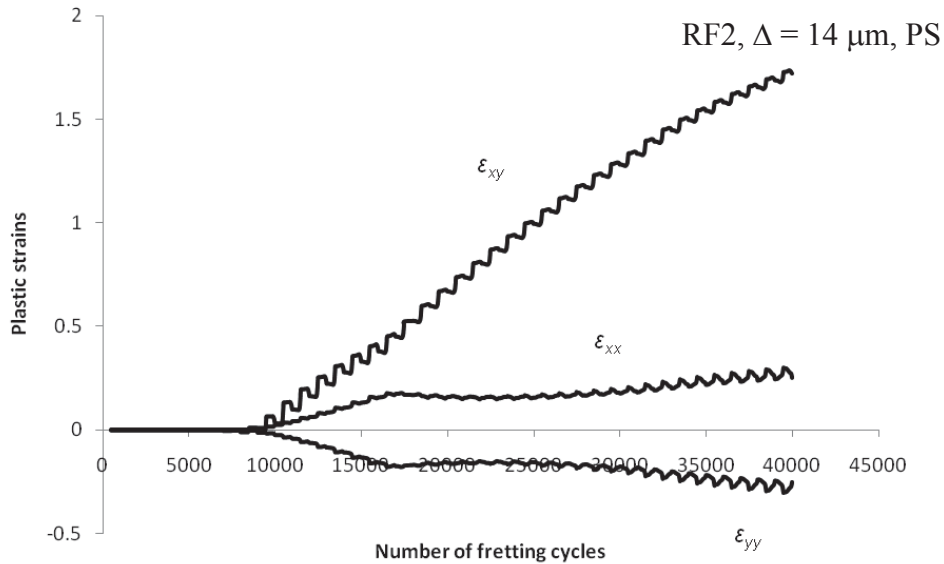
Fig. 21. Predicted evolutions of contact pressure for RP2 and RPF for 14 μm half-stroke.

1
2

3
4
5
6
7
8

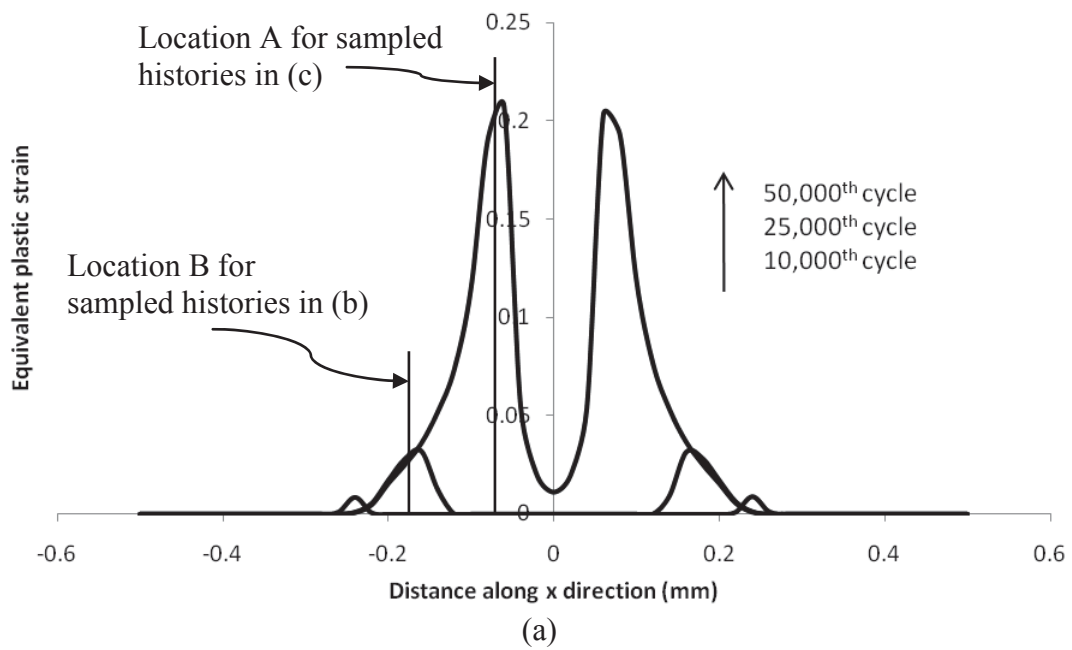


(a)

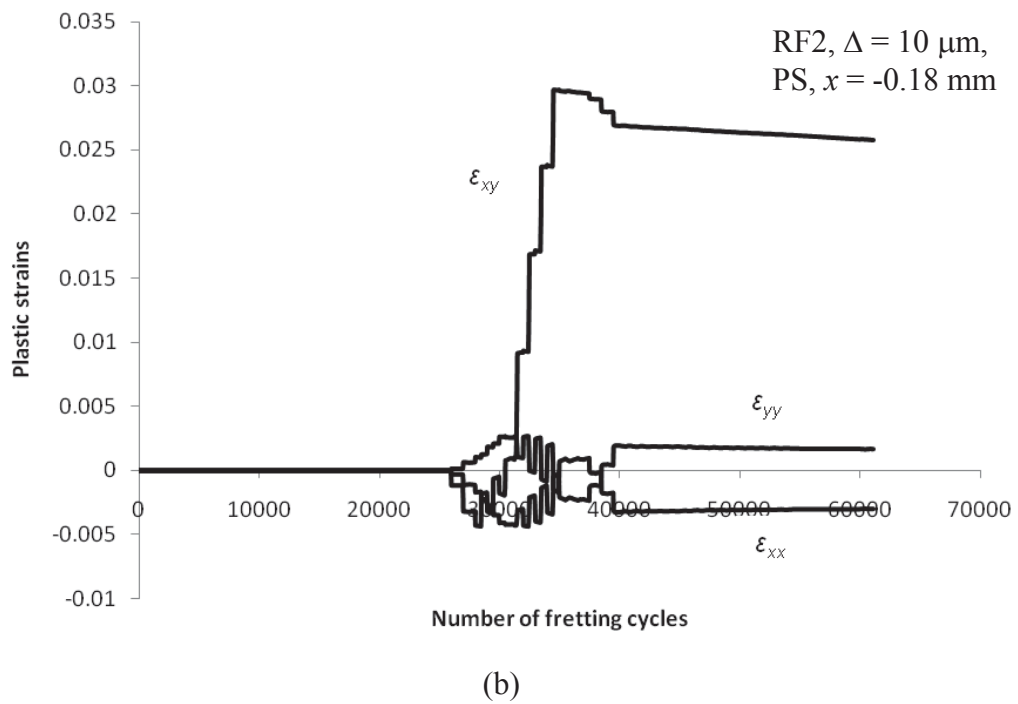


(b)

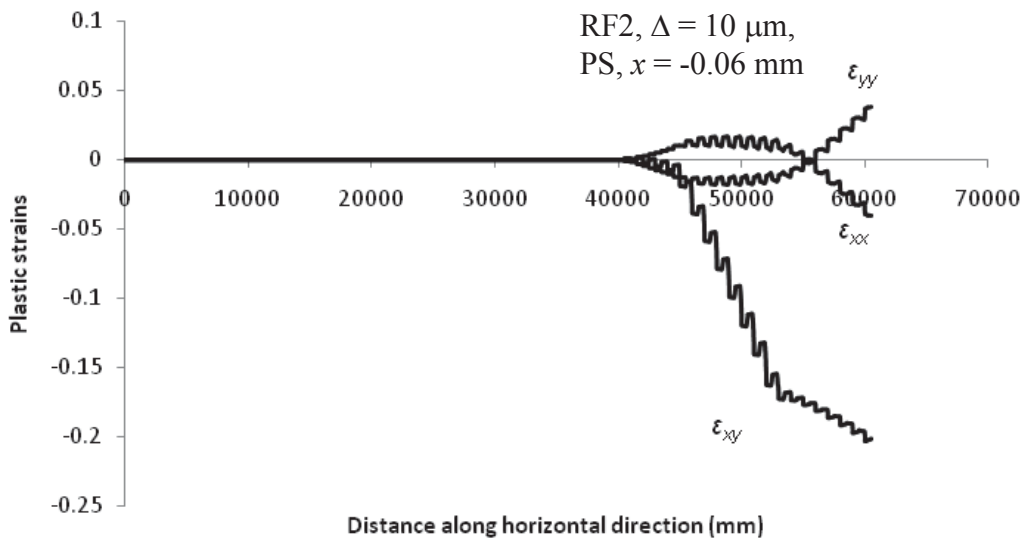
Fig. 22. (a) Predicted evolution of accumulated equivalent plastic strain distribution and (b) plastic strain histories at $x = 0.06$ mm [Point A in (a), initially in stick zone and after 15,000 cycles at the stick-slip interface] in RF2 for $\Delta = 14$ μm



1
2
3

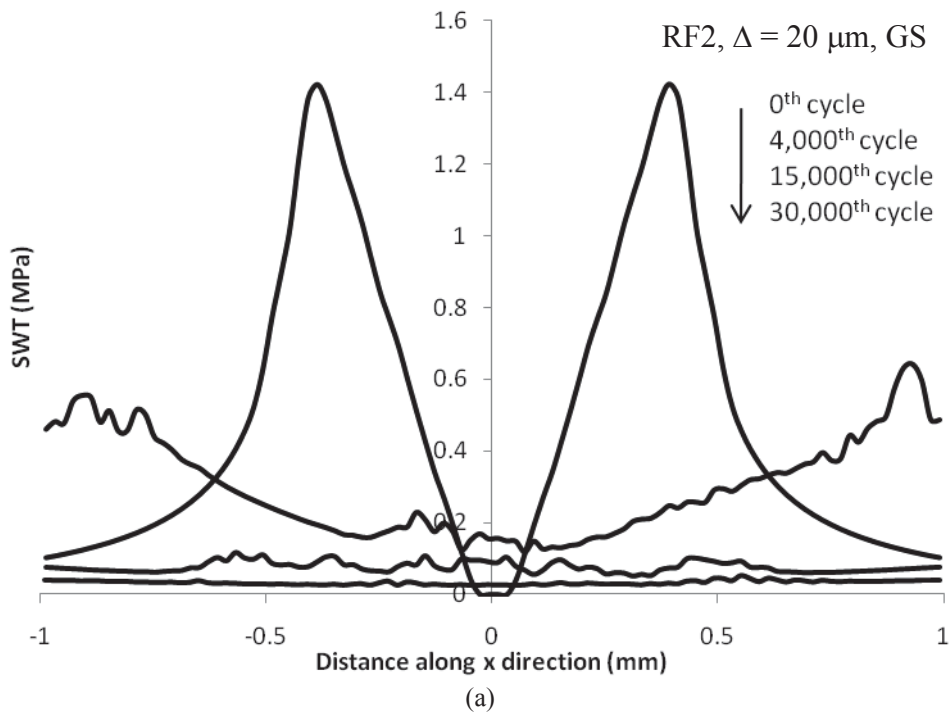


4
5



(c)

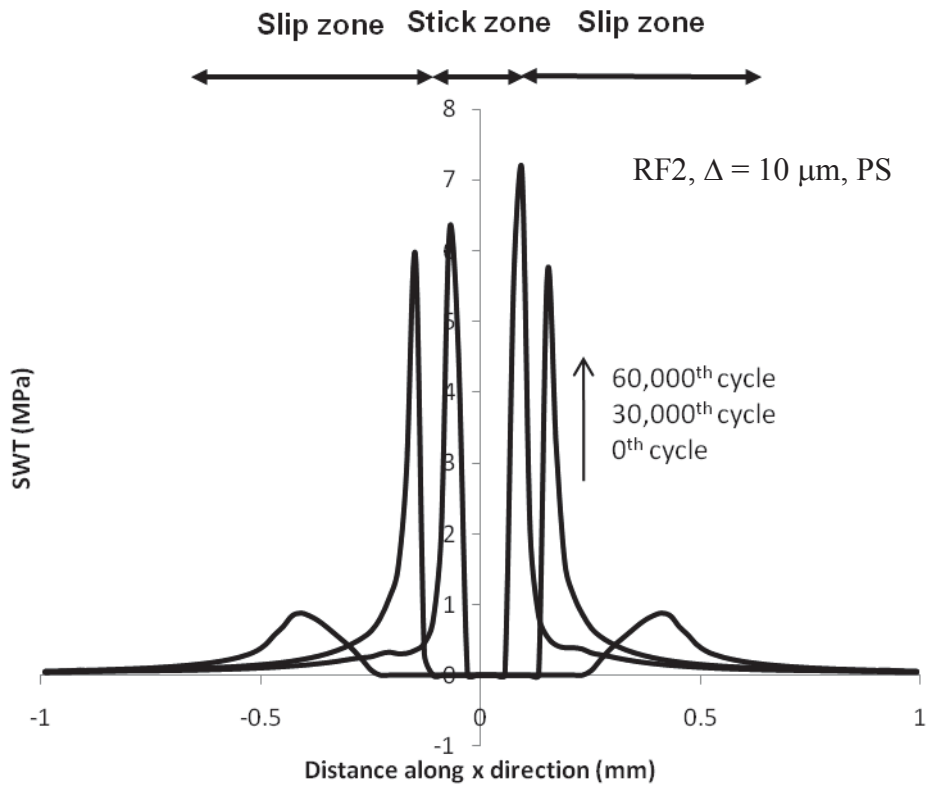
Fig. 23. Predicted plastic strain evolutions in RF2 for $\Delta = 10 \mu\text{m}$: (a) accumulated equivalent plastic strain distribution, (b) plastic strain components at $x = -0.182 \text{ mm}$ [point B in (a), initially in stick zone, after 50,000 cycle in slip zone] and (c) plastic strain histories at $x = -0.063 \text{ mm}$ [point A in (a), initially in stick zone, after 50,000 cycles in slip-stick interface].



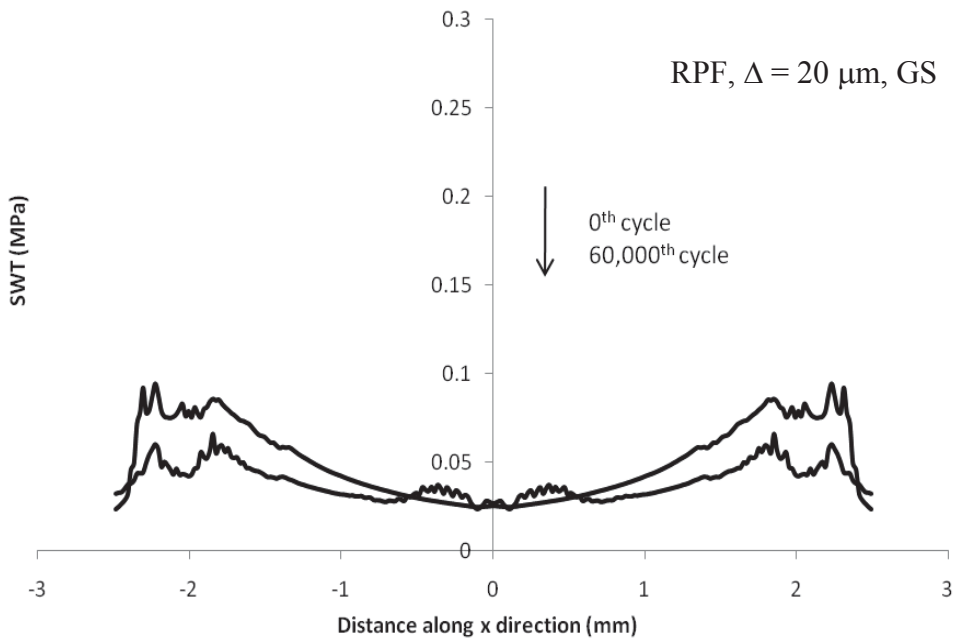
(a)

1
2
3
4
5
6
7
8
9

10
11
12



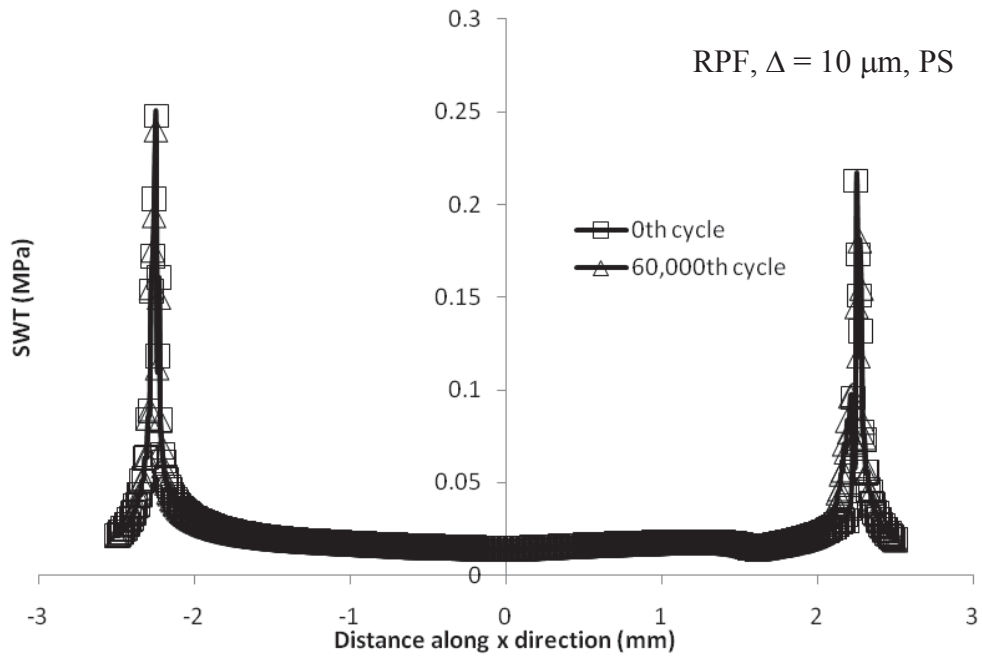
(b)



(c)

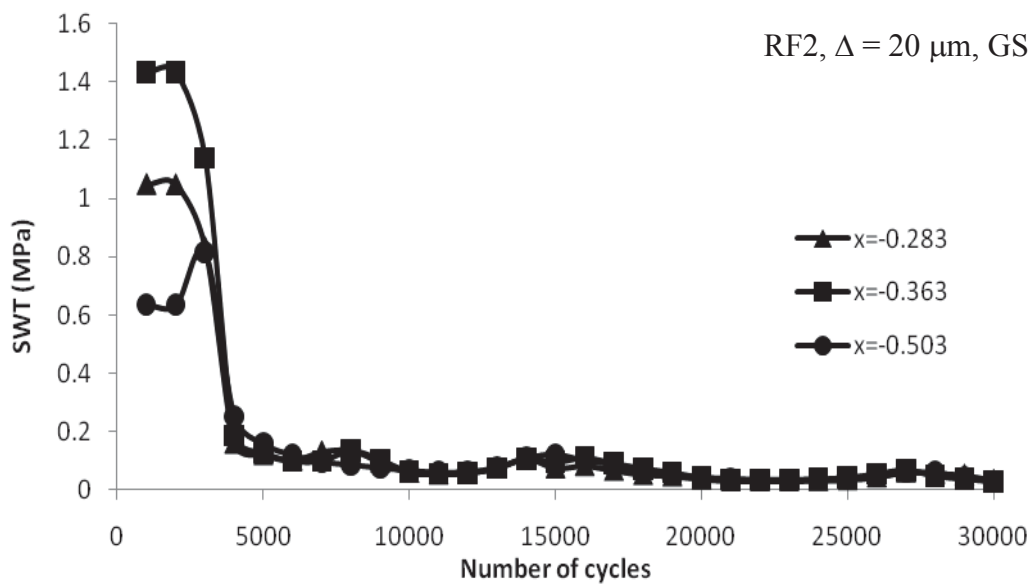
1
2
3

4
5
6



(d)

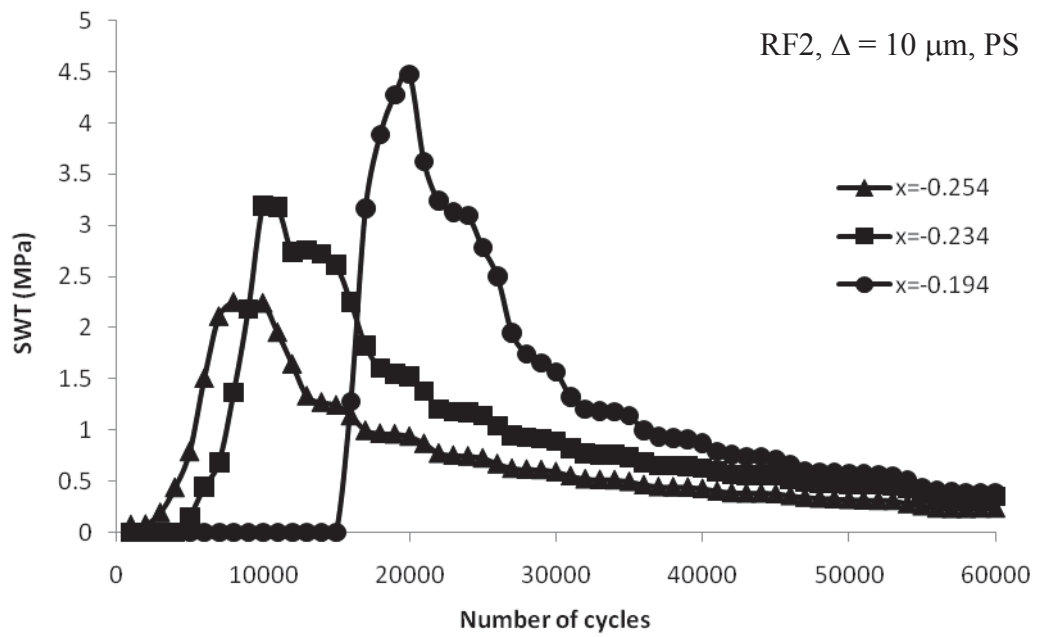
Fig. 24. Predicted evolutions of critical-plane SWT for: (a) RF2, 20 μm half-stroke (b) RF2, 10 μm half-stroke (c) RPF, 20 μm half-stroke (d) RPF, 10 μm half-stroke.



(a)

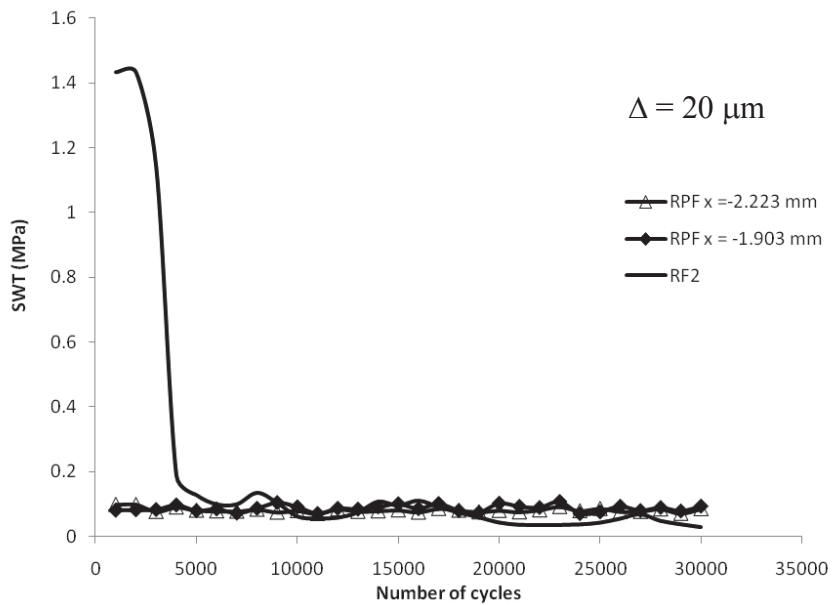
1
2
3
4
5
6

7
8



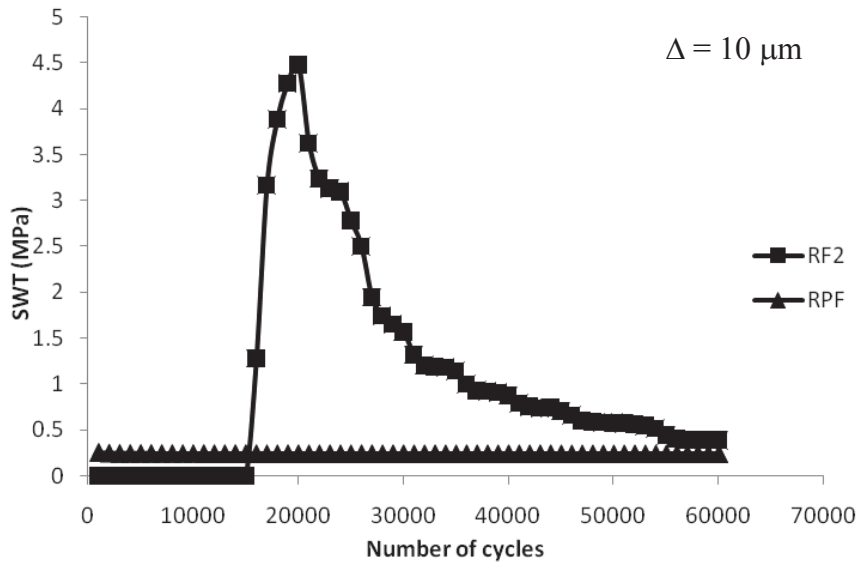
1
2
3
4
5
6

(b)
Fig. 25. Predicted evolution of critical-plane SWT with fretting cycles for: (a) RF2, 20 μm half-stroke (b) RF2, 10 μm half-stroke (c) RPF, 20 μm half-stroke and (d) RPF 10 μm half-stroke.



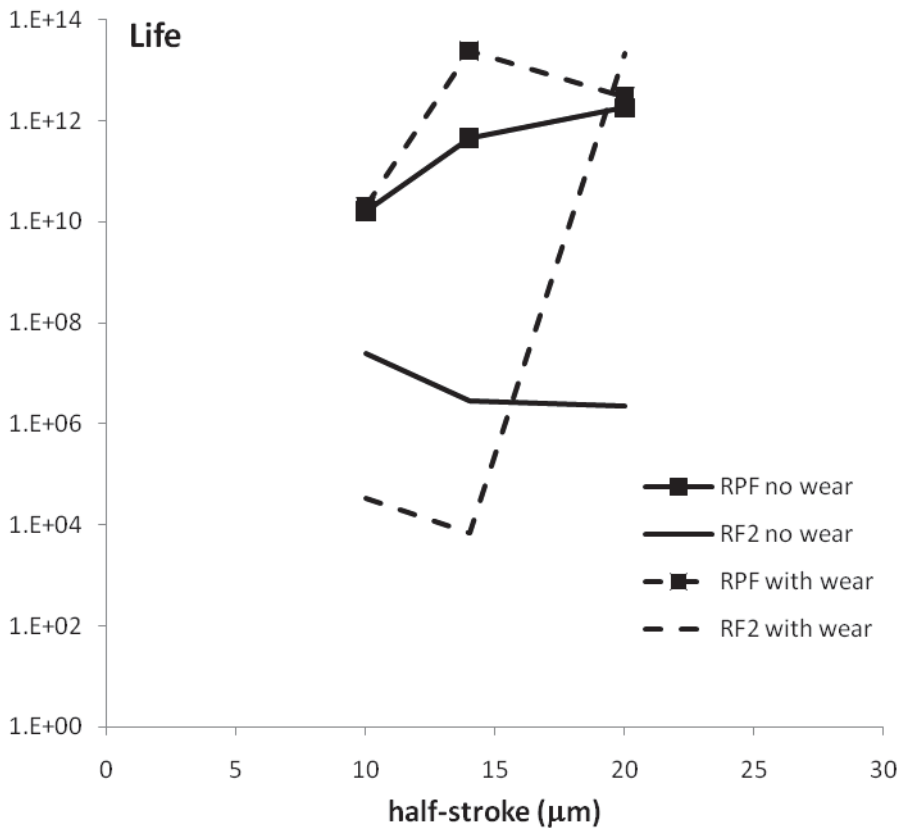
7
8

(a)



1
2
3
4
5

(b)
Fig. 26. Comparison of predicted crack nucleation performance of round on flat (RF2) and rounded punch on flat (RPF) in terms of critical-plane SWT evolution for: (a) 20 μm half-stroke, and (b) 10 μm half-stroke.



6
7
8
9

Fig. 27. Comparison of predicted crack nucleation performance of round on flat (RF2) against rounded punch on flat (RPF) as a function of half-stroke, for with wear and without wear assumptions.

Table

1 Tables

2 Table 1. Table of FE models for different fretting geometries studied.

Model	Pad type	Key dimensions	Test rig and source
RF1	Cylindrical pad	Pad radius, 6 mm	University of Nottingham test rig, e.g. [20]
RF2	Cylindrical pad	Pad radius, 50.8 mm	USAF test rig, e.g. [28]
RPF	Rounded punch pad	See Fig 1	USAF test rig, e.g. [28]

3

4 Table 2. Conditions of fretting tests of cylinder on flat arrangement (RF1).

Test no.	Normal load (N/mm)	Applied half-stroke, Δ (μm)	Slip regime
1	50	40	GS
2	100	22.6	PS

5

6 Table 3. Conditions of fretting analysis of RF2 and RPF arrangements.

Arrangement	Analysis no.	Normal load (N/mm)	Applied half-stroke, Δ (μm)	Slip regime
RF2	3	208	7	PS
	4	208	10	PS
	5	208	14	PS
	6	208	20	GS
RPF	7	208	7	PS
	8	208	10	PS
	9	208	14	GS
	10	208	20	GS

7

8 Table 4. SWT constants for Ti-6Al-4V corresponding to 10 μm crack nucleation (from Madge et al. [18] and [20])

σ_f' (MPa)	b	ϵ_f'	c
1817.2	-0.0978	0.841	-0.688

9

10

11

12

13

14